

Role of intrinsic and extrinsic defects in H implanted hydrothermally grown ZnO

Cite as: J. Appl. Phys. **126**, 125707 (2019); <https://doi.org/10.1063/1.5115597>

Submitted: 21 June 2019 . Accepted: 07 September 2019 . Published Online: 26 September 2019

R. Schifano , R. Jakiela , A. Galeckas , K. Kopalko, F. Herklotz, K. M. H. Johansen , and L. Vines 

COLLECTIONS

Paper published as part of the special topic on [Defects in Semiconductors 2020](#)

Note: This paper is part of the Special Topic on Defects in Semiconductors 2020.



View Online



Export Citation



CrossMark

ARTICLES YOU MAY BE INTERESTED IN

[Effects of InAlN underlayer on deep traps detected in near-UV InGaN/GaN single quantum well light-emitting diodes](#)

Journal of Applied Physics **126**, 125708 (2019); <https://doi.org/10.1063/1.5122314>

[Conduction mechanisms in ZnO nanowires based Schottky diode grown under an electric field](#)

Journal of Applied Physics **126**, 124501 (2019); <https://doi.org/10.1063/1.5117171>

[Compositional accuracy in atom probe tomography analyses performed on III-N light emitting diodes](#)

Journal of Applied Physics **126**, 124307 (2019); <https://doi.org/10.1063/1.5113799>



Lock-in Amplifiers

Zurich Instruments

Watch the Video

Role of intrinsic and extrinsic defects in H implanted hydrothermally grown ZnO

Cite as: J. Appl. Phys. 126, 125707 (2019); doi: 10.1063/1.5115597

Submitted: 21 June 2019 · Accepted: 7 September 2019 ·

Published Online: 26 September 2019



R. Schifano,^{1,a)} R. Jakiela,¹ A. Galeckas,² K. Kopalko,¹ F. Herklotz,³ K. M. H. Johansen,² and L. Vines²

AFFILIATIONS

¹Institute of Physics, Polish Academy of Sciences, Al. Lotników 32/46, 02-668 Warsaw, Poland

²Department of Physics/Center for Material Science and Nanotechnology, University of Oslo, P.O. Box 1048 Blindern, N-0316 Oslo, Norway

³Institute of Applied Physics, Technische Universität Dresden, 01062 Dresden, Germany

Note: This paper is part of the Special Topic on Defects in Semiconductors 2020.

a) Electronic mail: schifano@ifpan.edu.pl

ABSTRACT

The impact of hydrogen in ZnO is revealed by combining reaction dynamics calculations with temperature dependent Hall (TDH), photoluminescence, and secondary ion mass spectrometry measurements performed on H, ²H, and He implanted ZnO. H and ²H box profiles with a concentration ranging from $\sim 3 \times 10^{17} \text{ cm}^{-3}$ to $\sim 10^{19} \text{ cm}^{-3}$ and He to produce as much as damage as in the [H] $\sim 3 \times 10^{17} \text{ cm}^{-3}$ case were implanted in the samples. The formation of Li lean regions has been observed for [²H] $< 10^{19} \text{ cm}^{-3}$ after annealing at 400 °C. This is attributed to Li_i presence consequent to the diffusion of Zn_i created during the H/²H implantation process. Results extracted from the TDH measurements performed prior to the annealing at 400 °C evidence that Li_i contributes to an increase in carrier concentration up to $\sim 10^{17} \text{ cm}^{-3}$ by providing a donor level with an activation energy of $\sim 40 \text{ meV}$ and thus is very close to the value of $\sim 47 \text{ meV}$ expected for H in the oxygen site. The reaction dynamics analysis evidences that the amount of Li_i introduced is decreasing at higher H implantation doses as a result of increasing V_{Zn} and H-V_{Zn} retrapping, reactions in which Li_i is competing with H. Overall, due to Li_i formation as well as the presence of Al the maximum percentage of the implanted H or ²H acting as a donor in the investigated range is found to be $\leq 2\%$, which is considerably lower than previously reported.

Published under license by AIP Publishing. <https://doi.org/10.1063/1.5115597>

I. INTRODUCTION

Hydrogen in ZnO has been widely studied in the quest to achieve *p*-type conductivity since, on the basis of *ab initio* calculations, it has been proposed as responsible for the unintentional *n*-type conductivity of the material when incorporated on an interstitial bond-centered lattice site (H_{BC}).¹ Experimentally, first indications of H donor activity were attributed to hydroxyl ions formed at oxygen ion sites, and an activation energy of $\sim 50 \text{ meV}$ was reported.²⁻⁴

More recently, a second H related shallow donor configuration has been theoretically proposed: a multicentered bond H (H_O) that can be visualized as an O vacancy (V_O) with a single fourfold coordinated H atom near the center.⁵ Evidence of the presence of two hydrogen related donors with activation energies $\sim 53 \text{ meV}$ and $\sim 47 \text{ meV}$ assigned to H_{BC} and H_O has been found by combining photoluminescence (PL) spectroscopy, photoconductivity

measurements, Raman scattering, and Fourier Transform Infrared (FTIR) Spectroscopy.⁶ However, in other studies based on temperature dependent Hall (TDH) measurements and electron paramagnetic resonance (EPR) spectroscopy or PL measurements, only a level $\sim 40 \text{ meV}$ below the conduction band edge, E_C , was assigned to an H related donor with the second one in the 55–66 meV attributed to Al or left unassigned.^{7,8} Moreover, evidence of H passivation of ionized compensating acceptors and introduction of a shallow donor level has also been reported in studies based solely on TDH measurements⁹ or supported by PL and FTIR,^{10,11} with a variety of activation energies that are overall varying in the ~ 53 – 28 meV range. Secondly, in the case of implanted H, the activated percentage acting as a donor has been reported to vary in the $\sim 30\%$ – 65% range and assigned to H_O.^{9,11} However, in these works, the thermal stability of the donor assigned to H has been found to be $< 400 \text{ °C}$ even though H_O is reported to be thermally stable up to $\geq 500 \text{ °C}$.^{5,6,12,13}

Furthermore, possible interactions of H with the defects created during implantation were discussed only qualitatively.

Meanwhile, considerable progress in understanding intrinsic point defects features as well as their interaction with H has been made. As an example, proof for zinc interstitials (Zn_i) diffusion has been obtained by monitoring Li. That is, the occurrence of Li-depleted regions has been observed as a consequence of the Zn_i interstitialcy diffusion process, that is, converting substitutional Li atoms in the Zn site (Li_{Zn}) into highly mobile interstitial ones (Li_i).¹⁴ Furthermore, the strong interaction between zinc vacancy (V_{Zn}) and H has been more deeply investigated by providing both experimental and theoretical evidences of the H_n-V_{Zn} complexes formation with $n = 1, 2, 3$.^{15–20} In addition, it has been shown that significant V_{Zn} clustering with V_O is starting already at temperatures $\geq 100^\circ\text{C}$.²¹ Indeed, the formation of H-filled bubbles has been detected by positron annihilation spectroscopy (PAS) in H implanted samples after annealing in the 200–500 °C range.²² This mechanism, if present, is relevant in studies like the one here presented since a large amount of H might be potentially allocated in such voids and therefore, for example, not take part in the donor formation.

The purpose of this work is to tackle once more the topic of H implantation into hydrothermally grown ZnO (HT-ZnO) in light of the above mentioned recent results. This article is organized as follows: in Secs. II and III, the experimental details as well as the theoretical background on which the analysis of the data is based are provided. Then, in Sec. IV, the experimental results are discussed. There, a reaction kinetics analysis that includes the relevant intrinsic point defects introduced during implantation is combined with the results extracted from TDH and PL measurements and a consistent scenario is proposed. It is shown that the carrier concentration increase is the result of an interplay between H, Zn_i , and V_{Zn} introduced during the implantation as well as Al and Li already present in the material; Sec. IV ends with an upper limit estimate for the H donor activity that is found to be $\leq 2\%$, that is, H might not be the primary cause of the carrier concentration increase observed in similar experiments. Finally, in the Appendix, details on the multilayer analysis necessary to extract from the raw TDH measurements the implanted layers electrical characteristics are provided.

II. EXPERIMENTAL DETAILS

Four square 5×5 mm wide samples, labeled hereafter as A, B, C, and D, were obtained from a HT SPC Goodwill wafer with room temperature (RT) resistivity, ρ , equal to ~ 0.7 k Ω cm. Similarly, three square samples, A', B', and C', were cut from a HT Tokyo Denpa Co. Ltd. wafer with $\rho \sim 3$ k Ω cm at RT. Afterward, all the samples were cleaned in a ultrasonic bath with acetone and ethanol and finally rinsed in deionized water. Samples A and A' were kept as references, while the remaining underwent implantation. H and ^2H were implanted through a $15\ \mu\text{m}$ thick aluminum foil placed on the O-face and Zn-face of the samples originating from the SPC Goodwill and Tokyo Denpa Co. Ltd. wafers, respectively. A series of three nuclei energies were used: 1.02, 1.07, 1.12 MeV and 1.26, 1.31, 1.37 MeV for H and ^2H , respectively. The doses and the energies were chosen according to TRIM

simulations²³ to obtain box profiles extending $\sim 2\ \mu\text{m}$ in the samples with: $[H] \sim 2 \times 10^{17}\ \text{cm}^{-3}$, $[H] \sim 2 \times 10^{18}\ \text{cm}^{-3}$, $[^2\text{H}] \sim 10^{18}\ \text{cm}^{-3}$, and $[^2\text{H}] \sim 10^{19}\ \text{cm}^{-3}$ in B, C, B', and C', respectively.^{24–26} To study the bare effect of implantation damage 25, 80, 170, 290, and 440 keV, He ions were implanted through the O-face in sample D. Doses and energies were selected to produce approximately the same V_O and V_{Zn} concentration compared to that of sample B. The samples implantation conditions and H/ ^2H concentrations as extracted from SIMS measurements (cf. Fig. 1) are summarized in Table I. Postimplantation annealing at 200 °C has been found necessary to obtain layers with optimal electrical characteristics in previous works.^{9,11,27} Therefore, 30 min long annealing in N_2 flow at 200 °C was performed on all samples. An additional anneal of 30 min in air at 200 °C for samples A, B, C, and D was carried out in order to

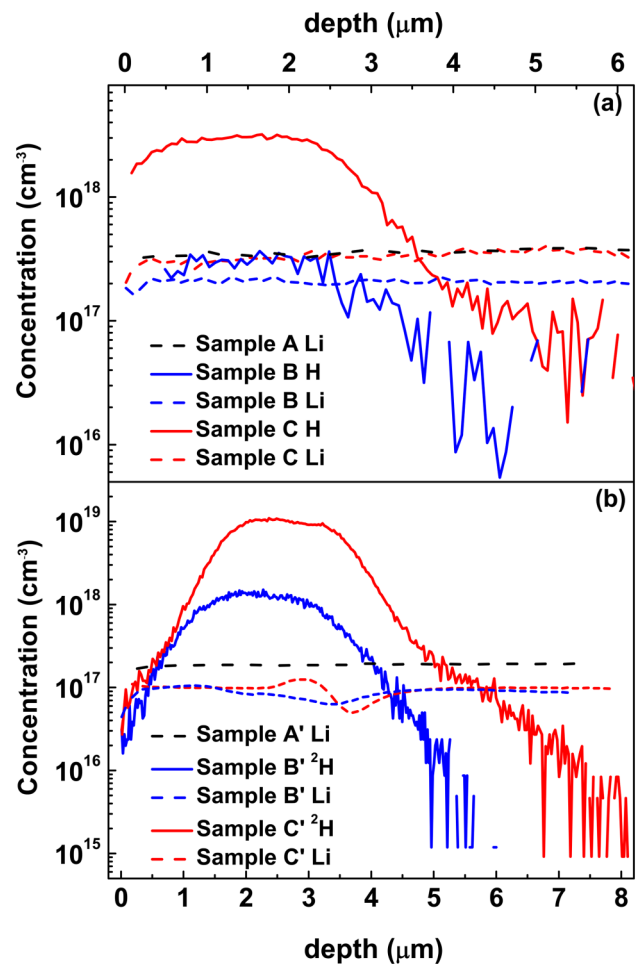


FIG. 1. (a) H (after background subtracting) and Li chemical profiles and (b) ^2H and Li chemical profile for samples B, C and B', C', respectively. The Li chemical profile for the unimplanted samples A and A' is also included in (a) and (b), respectively. All concentrations were measured after the corresponding annealing at 200 °C.

TABLE I. Samples overview.

| Sample | Implanted species and measured concentration | Implanted/ examined face |
|--------|--|--------------------------|
| A | Reference | O-face |
| B | [H] $\approx 3 \times 10^{17} \text{ cm}^{-3}$ | O-face |
| C | [H] $\approx 3 \times 10^{18} \text{ cm}^{-3}$ | O-face |
| D | [He] $\sim 1.8 \times 10^{16} \text{ cm}^{-3}$ | O-face |
| A' | Reference | Zn-face |
| B' | [^2H] $\approx 10^{18} \text{ cm}^{-3}$ | Zn-face |
| C' | [^2H] $\approx 10^{19} \text{ cm}^{-3}$ | Zn-face |

reduce the surface conductivity.²⁸ Subsequently, Ohmic contact was formed by soldering small In dots on the implanted/reference face side. Afterward, TDH measurements were performed in the Van Der Pauw configuration with a probing magnetic field strength of 1 T by using a LakeShore 7604 apparatus. Measurements were undertaken with the samples in dark immersed in an He bath varying the temperature from 330 K to 10 K.

The concentrations were measured by SIMS with a Cameca IMS 7f microanalyzer. A primary beam of 15 keV Cs^+ ions and of 10 keV O_2^+ ions and corresponding implanted reference samples were used for determining the H or ^2H and the Li, Al, Ga, and In chemical profiles, respectively. The crater depths were subsequently measured with a Dektak 8 stylus profilometer and a constant erosion rate was assumed for depth calibration of the impurity profiles.

Subsequently, with the Cameca IMS 7f microanalyzer, by using a primary beam of 10 keV O_2^+ ions, two craters $\sim 300 \times 300 \mu\text{m}$ wide were made in all H and ^2H implanted samples. For each sample, the craters depth was chosen according to the SIMS measurements to expose to air an H or ^2H uniformly implanted and a virgin area, respectively. The craters were probed in spatially-resolved PL measurements using the 325 nm line of a HeCd cw-laser (6 mW) as an excitation source corresponding to a penetration depth $\alpha^{-1} \approx 100 \text{ nm}$.²⁹ The laser beam was focused to a full width at half maximum (FWHM) diameter of $\sim 40 \mu\text{m}$, while the spectral resolution of the detection system was better than 0.2 nm. The samples were mounted in a closed-cycle He cryostat and measured at 10 K in this case. Higher resolution PL measurements on the samples surface were performed with a liquid He bath cryostat at 4.2 K. The typical excitation power and resolution was 2 mW and 0.025 nm, respectively. A single 1200 rules/mm grating monochromator ($f = 1 \text{ m}$) was used and calibrated against Hg lamp lines.

Finally, Li redistribution in the samples was studied by annealing subsequently the samples for 30 min in N_2 flow in the 400–700 °C range. SIMS profiles after each annealing step were acquired, in this case, with a Cameca IMS 6f microanalyzer using a primary beam of 5.5 keV Cs^+ ions or of 8 keV O_2^+ ions and the depth was measured with a Dektak 6M stylus profilometer assuming a constant erosion rate. Overall, since, as previously reported (see Ref. 30), [Li] lateral fluctuations are expected in the samples, at least two different points for each sample were analyzed to extract [Li] both after the 200 °C and 400 °C annealing.

III. DETAILS ON THE ANALYSIS

A. Reaction dynamics analysis

The kinetic evolution of the selected reactions discussed in Subsection IV A has been modeled according to the theory for diffusion limited reactions.³¹ In this approach, if an uniform distribution of neutral defects is assumed, the time dependence, t , of the $A + B \rightarrow AB$ reaction is quantitatively described by the differential equation³²

$$\frac{d[A]}{dt} = \frac{d[B]}{dt} = -4\pi r_0^* D[A][B] \left[1 + \frac{r_0^*}{\sqrt{\pi D t}} \right], \quad (1)$$

where $D = D_A + D_B$ is the sum of the diffusion coefficients of species A, D_A and B, D_B , and r_0^* is the capture radius usually set to a typical interatomic distance in the lattice (0.5 nm in our case cf. Table III).³³ On the other hand, if a Coulomb attractive potential is present between the two reacting species with charge q_A and q_B r_0^* , indicated in this case as r_{AB}^* , equals³²

$$\frac{|q_A q_B|}{4\pi \epsilon_0 \epsilon_r r_{AB}^*} = k_B T, \quad (2)$$

with k_B , ϵ_0 , ϵ_r and T being the Boltzmann constant, vacuum, and relative permittivity constant and temperature, respectively.

B. Analysis of the temperature Hall effect measurements

The H and ^2H chemical profiles in samples B, C and B', C' are shown in Figs. 1(a) and 1(b), respectively. Reasonable agreement with the concentrations anticipated by the TRIM simulations is found (cf. Fig. 1 and Table I with the values listed in Sec. II), while the experimental extensions of the ^2H box profiles appear to be significantly larger than expected suggesting residual channeling in this case. Because of the H or ^2H presence, the samples are inhomogeneous along the implantation direction. Furthermore, surface conductivity has been found to affect C and C' (see Fig. 10). Hence, to extract the electrical characteristics of the H or ^2H implanted region from the TDH measurements, a multilayer analysis is necessary. This approach relies on the knowledge of the implanted layer extension, d_{impl} , as described in detail in the Appendix. The depth interval where the conditions $[\text{H}] > [\text{Li}]$ and $[^2\text{H}] > [\text{Li}]$ hold for samples B, C and B', C', respectively, has been assumed as d_{impl} . This assumption is *a posteriori* justified from the results discussed in Subsection IV A. The d_{impl} values obtained by comparing the H or ^2H profiles with the Li concentration also shown in Figs. 1(a) and 1(b) are reported in Table VI. Successively, the data extracted from the multilayer analysis have been analyzed as described in Ref. 30. This approach has been shown, by comparison with thermal admittances spectroscopy (TAS) and deep level transients spectroscopy, to properly describe the prevalent electrical defects present in similar samples.^{34,35} In detail, the carrier concentration, $n_{imp}(T)$, i.e., the H or ^2H implanted layer Hall carrier concentration, n_{H}^i , multiplied for the Hall scattering factor, r_H , has been modeled by assuming the presence of a fully ionized single charged acceptor (A) with concentration N_A^- and three

TABLE II. Li, Al, Ga, and In concentrations in 10^{16} cm^{-3} for samples A, B, C and A', B', C' as obtained by SIMS. In the case of samples B, C, B', and C', the listed Li concentrations correspond to the samples' bulk level, i.e., measured beyond the H or ^2H implanted region.

| | Li | Al | Ga | In |
|----|-------------|-----------------|-----------------|--------------|
| A | 40 ± 10 | 34 ± 3 | ≤ 0.2 | ≤ 0.02 |
| B | 20 ± 6 | 16 ± 1 | 0.4 ± 0.1 | ≤ 0.004 |
| C | 36 ± 7 | 14 ± 2 | 0.8 ± 0.2 | ≤ 0.01 |
| A' | 14 ± 6 | 0.4 ± 0.2 | 0.2 ± 0.1 | ≤ 0.003 |
| B' | 10 ± 4 | 0.15 ± 0.06 | 0.14 ± 0.05 | ≤ 0.005 |
| C' | 11 ± 5 | 0.2 ± 0.1 | 0.2 ± 0.1 | ≤ 0.004 |

s-like donors (D_i , $i = 1, 2, 3$) with negligible temperature dependence of the energy level positions. Hereafter, the type D_i donor activation energy and concentration are labeled as E_{D_i} and N_{D_i} , respectively. As seen from Table II, Al and Ga provide the dominant background concentration of donors in the material. Published results indicate that the majority of Al and Ga reside in their donor configuration (Al_{Zn} and Ga_{Zn}), with only a minor part of it ($\leq 10\%$) that is possibly compensated by V_{Zn} .^{36–38} Thus, in the simulations, N_{D_2} has been limited to $([\text{Al}] + [\text{Ga}])$ as measured by SIMS, while N_{D_1} , N_{D_3} , E_{D_1} , E_{D_2} , E_{D_3} , and N_A^- have been treated as fitting parameters. The H or ^2H implanted layer mobility, $\mu_{\text{imp}}(T)$, equal to the Hall mobility, μ_H , divided by r_H , has been modeled in the relaxation time approximation.³⁹ Finally, the unknown quantities have been evaluated by simultaneously fitting $n_{\text{imp}}(T)$ and $\mu_{\text{imp}}(T)$. In addition, here it is worth mentioning that few variations have been introduced compared to previous work (Refs. 30 and 34). First of all, $(6.05 \pm 0.15) \text{ eV}$ has been used as value for the deformation potential since it is closer to recently published theoretical calculations than the one earlier adopted.^{40,41} Furthermore, implantation damaging might promote formation of extended defects like dislocations and voids as mentioned in Sec. I and discussed in detail in Sec. IV. Hence, the dislocation density, N_{dis} , has been considered as a free fitting parameter. On the other hand, voids have been modeled as thick impenetrable volumes and, therefore, a space-charge scattering (SC) contribution has been added to the scattering mechanisms listed in Ref. 30. This has been achieved by including a relaxation time, $\tau_{\text{SC}}(E)$, with dependence on the electron energy, E , equal to³⁹

$$\tau_{\text{SC}}(E) = \frac{(m^*)^{1/2}}{\sqrt{2}N_{\text{SC}}\sigma_{\text{SC}}E^{1/2}}, \quad (3)$$

where m^* is the electron effective mass in ZnO, N_{SC} , and σ_{SC} are the concentration of space-charge scattering centers and cross section, respectively. The last two quantities have been assumed as one fitting parameter, R_{SC} , equal to $(N_{\text{SC}} \times \sigma_{\text{SC}})^{-1}$. Finally, since the Falicov-Cuevas ionized impurity scattering relaxation time describes the charged centers scattering contribution in highly compensated semiconductors, its use has been limited to A, B, and A' due to the anticipated presence of a high compensation ratio in these cases.⁴² For the remaining samples, i.e., B', C, and C', the Brooks-Herring ionized impurity relaxation time was chosen, since it is more appropriate

for describing this scattering mechanism in low compensated semiconductors.⁴³

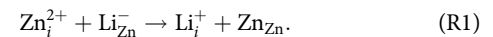
C. Analysis of the photoluminescence measurements

The nature of peaks present in the PL spectra has been established on the basis of their localization energy and comparison with the energy interval where excitons bound to ionized donors (D^+X), neutral donor bound excitons (DX), two electron satellite ($DX\text{-TES}$), and longitudinal optical phonon replica recombination ($DX\text{-LO}$) are expected to occur in ZnO.⁴⁴ The activation energy corresponding to the DX recombination has been calculated using the ‘‘Haynes’’ rule and labeled as E_{DX}^H .^{44,45} When the $DX\text{-TES}$ recombination signature was also clearly distinguishable, a second estimate, E_{DX}^{TES} , has been determined by employing the energy distance between DX and $DX\text{-TES}$, corresponding to the ground and the $2P_{x,y}$ excited state of the donor, respectively.⁴⁴ Finally, the energy distance between DX and $DX\text{-LO}$ has also been calculated to verify the energy of the longitudinal optical phonon involved, $\hbar\omega_{\text{op}}^{\text{PL}}$.

IV. EXPERIMENTAL RESULTS AND DISCUSSION

A. Effect of H/ ^2H implantation on the Li profiles and reaction dynamics simulations

It has been shown experimentally that the prevailing configuration for Li in $HT\text{-ZnO}$ is Li_{Zn} where it acts as an acceptor.^{34,46–48} Furthermore, the same studies provide evidence that Li_{Zn} is the main compensating center in the material. In our case, Li profiles after the H implantation and successive 200°C annealing are found to be either uniform or progressively decreasing towards the surface in the case of samples B and C, respectively, as can be seen in Fig. 1(a) [these profiles are redisplayed in Figs. 2(a) and 2(b) as well]. On the other hand, clear Li redistribution has been observed in the B'–C' series as can be seen in Figs. 1(b), 2(c), and 2(d). This is pointing to the presence of Li_i . Indeed, the formation of Li_i is anticipated, since Zn_i is among the point defects produced during the implantation. The diffusion of Zn_i is occurring already at RT due to the very low migration barrier of $\sim 0.55 \text{ eV}$ and it is taking place by interstitialcy mechanism as noted in Sec. I.^{49,50} That is, Li_i can be formed in the implanted layers through the reaction^{14,51}



The reverse of (R1), corresponding to a Li_i kicking out a Zn_{Zn} , requires a calculated annealing temperature of $\sim 580^\circ\text{C}$ according to the transition state theory^{50,52} and, therefore, is not relevant in the temperature range here of main interest. A second annealing at 400°C in N_2 for 30 min has been performed on all samples with the temperature choice dictated by the previous studies mentioned in Sec. I where a $\sim 10^{17} \text{ cm}^{-3}$ carrier concentration drop was reported to occur after a similar treatment.^{9,11} The resulting Li SIMS profiles are also displayed in Fig. 2. It can be seen that evidence for the formation of a Li-depleted region has been observed in C and B'. In sample B, as can be seen by looking at Fig. 2(a), occurrence of Li redistribution is less discernible. However, we interpret the $< 5 \times 10^{16} \text{ cm}^{-3}$ decrease in Li concentration observed extending $\sim 2 \mu\text{m}$ from the surface to the same physical mechanism since it has

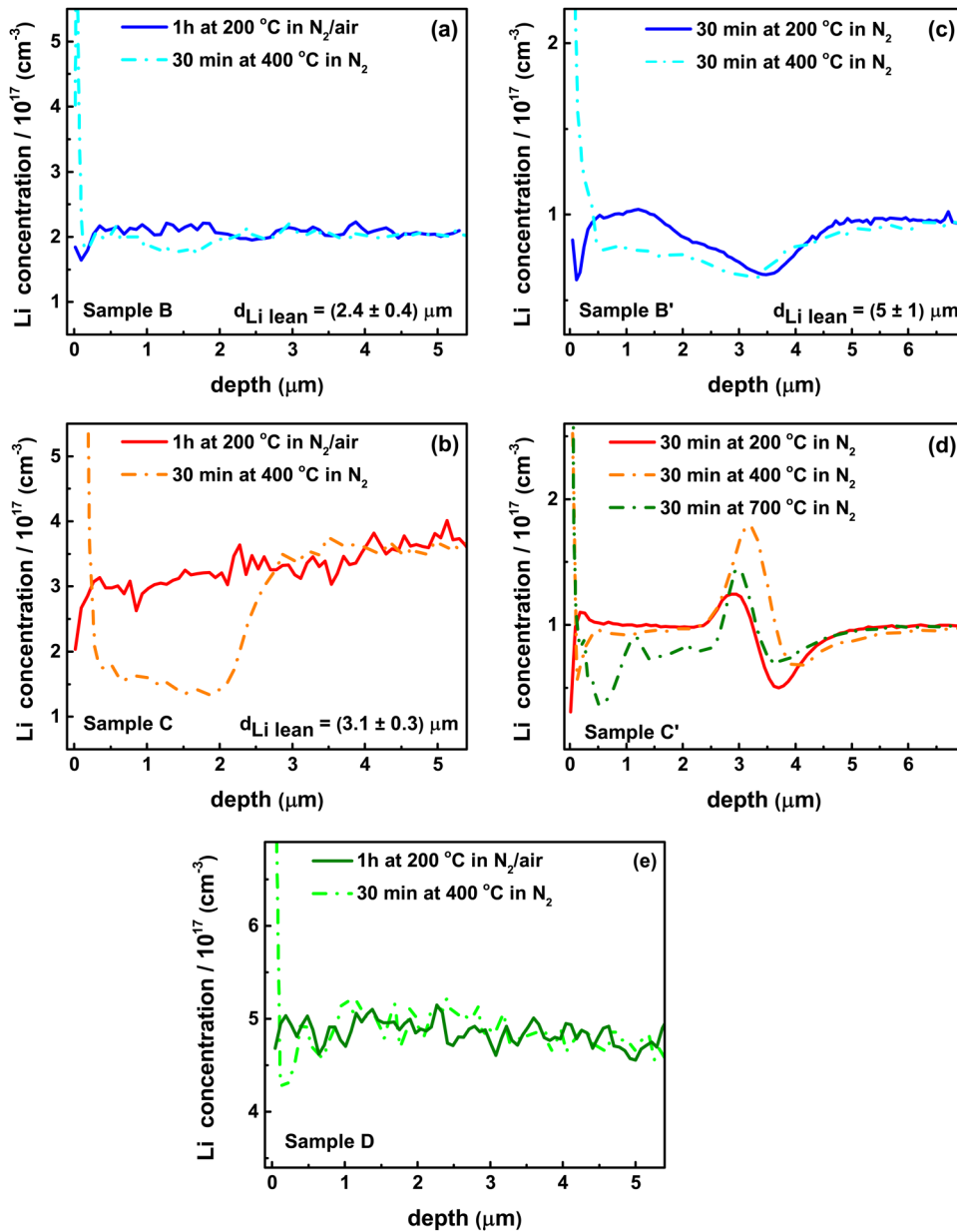


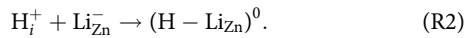
FIG. 2. (a), (b), (c), (d), and (e) SIMS Li profiles measured after the TDH measurements (solid lines) and successively to an annealing at 400 °C in N_2 for 30 min (dashed lines) for samples B, C, B', C', and D, respectively. In all cases, the Li profiles after the 400 °C annealing have been normalized to the Li bulk concentration. In the case of sample C', the Li distribution successive to an annealing at 700 °C in N_2 for 30 min is also included.

been observed in 3 different points of the sample and its width is in agreement with the H box profile dimensions, as discussed in detail hereafter. On the other hand, no clear indication of the presence of a similar Li lean region has been observed in samples C', D, A, and A' (with the latter two not included in Fig. 2).⁵³ Overall, considering that [Li] lateral fluctuations are present to compare Li profiles acquired prior and after the 400 °C annealing normalization to the Li bulk concentration has been adopted in presenting the data in Fig. 2 and both the scaling factor and the residual differences between the different points examined included in the analysis discussed hereafter. To quantify the amount of Li, the difference between Li level in the

bulk and in the H or 2H implanted region after the 400 °C annealing, quantity indicated as $[\Delta Li_i]^{exp}$ in the following, has been employed. This approach has been also used to establish the extension of the Li_i region, $d_{Li\ lean}$, with the results reported in Fig. 2 as well. By comparison with the d_{impl} values reported in Table VI, it can be seen that the Li lean extension corresponds to the region where the conditions $[H] > [Li]$ and $[^2H] > [Li]$ hold.

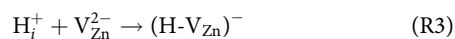
$[\Delta Li_i]^{exp}$ is exhibiting an unexpected dependence on the H/ 2H implanted concentration. That is, it is found to be equal to $(2.2 \pm 0.6) \times 10^{17} \text{ cm}^{-3}$ in sample C, while it is $\approx 10^{16} \text{ cm}^{-3}$ for C', despite a 3 times higher 2H dose is introduced in the latter pointing

to the occurrence of a limiting factor in high H implantation regimes. In addition, the comparison between the Li profiles of samples *B* and *D* acquired after the 400 °C annealing suggests that the Li_i presence is a by-product of the H and ^2H implantation. In order to understand the physical mechanism behind these dependences and perform a reactions dynamic analysis, the relevant reactions that involve Li and H, besides (R1), have to be individuated. *Ab initio* calculations forecast a strong interaction between H_i and Li_{Zn} through the reaction⁵⁴

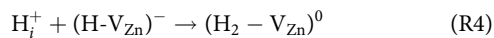


The formation of H- Li_{Zn} complexes is occurring already at RT due to the low migration barrier of H and ^2H of ~ 0.85 eV and, therefore, this process has to be included among the relevant reactions.⁵⁵

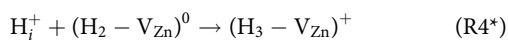
Furthermore, limiting the present discussion to point defects, besides Zn_i , also V_{Zn} , V_{O} , and oxygen interstitials (O_i) are produced during H and ^2H implantation and, while partly escaping the dynamic annealing (i.e., direct recombination of Frenkel pairs), might also participate in the reactions.⁵⁶ V_{Zn} s are practically immobile at RT.⁵⁰ Moreover, V_{Zn} s are theoretically anticipated to be deep double acceptors with the 1-/2- level being ≥ 1.4 eV below E_{C} . Therefore, they are expected to be double negatively charged in the H and ^2H implanted region.^{16,17,50} Furthermore, as anticipated in Sec. I H_n - V_{Zn} complexes, with $n = 1, 2, 3$ at least, are also expected to form already at RT due to the above mentioned low H_i^+ diffusion barrier.⁵⁰ Therefore, the reactions



and



have also been included in the simulations. On the other hand, the contribution of the additional reaction



is expected to be negligible on the time scale of interest due to the absence of Coulomb attraction (see Table III) as numerically proved hereafter. The reaction



TABLE III. Parameters used in solving the coupled differential equations corresponding to (R1)–(R6). Capture radii are in nm and diffusion coefficients in $\text{cm}^2 \text{s}^{-1}$ and evaluated at 300 K. In the case of the capture radii, the subscript corresponds to the charge state of the pair of defects involved in the reaction.

| | |
|----------------------------------|---|
| $r_0^* = 0.5$ | $D_{\text{Zn}_i} = 1.5 \times 10^{-13\text{a}}$ |
| $r_{+/-}^* = 6.7$ | $D_{\text{H}} = 1.9 \times 10^{-16\text{b}}$ |
| $r_{2+/-}^* = r_{2-/+}^* = 13.4$ | $D_{^2\text{H}} = 1.3 \times 10^{-16\text{b}}$ |

^aTaken from Ref. 49.

^bTaken from Ref. 55.

involves V_{O} that is not mobile at RT.⁵⁰ Furthermore, V_{O} s are anticipated to be neutral, considering that the 0/2+ charge state is occurring at ≥ 1 eV below E_{C} , while $[\text{V}_{\text{O}}]$ is $\sim [\text{V}_{\text{Zn}}]$ and therefore is also neglected in the first approximation. Concerning O_i , they are theoretically expected to exist in a split ($\text{O}_i^{\text{split}}$) and an octahedral configuration (O_i^{oct}), where the former is electrically neutral, while the latter is a double acceptor with the -/2- charge state transition occurring ≥ 1.8 eV below E_{C} .⁵⁰ The migration barrier for such defects is in the ~ 0.9 – 1.1 eV range, depending on the charge state, and could, therefore, be sufficiently mobile at RT. However, the reaction $\text{O}_i + \text{H}_{\text{O}}^+ \rightarrow \text{H}_i^+ + \text{O}_{\text{O}}$ relies on the H_{O}^+ production, i.e., it is, in the approach used here, a second order correction and has not been included. Here, it is worth pointing out that there is excellent agreement between the experimental values for the Zn_i diffusion activation energies mentioned above and their theoretical counterparts.^{49,50} Similarly, for H_i detailed studies clarified the cause behind the discrepancy among experimental migration barriers reported.^{55,57} On the contrary in the case of Li_i theoretical estimates are consistently in the 0.58–0.7 eV range,^{51,52,54} that is, Li_i is expected to be a fast diffuser in ZnO as also suggested in an early study.³ However, other published experimental values^{58,59} are ≥ 0.3 eV higher with the difference most probably related to the presence of interacting defects with also the Fermi level position possibly playing a role.^{51,58} Therefore, in the present analysis, the possibility that Li_i is already mobile at RT has been taken into account by including possible reactions involving Li_i while keeping its diffusivity, D_{Li_i} , as a fitting parameter. Close-by V_{Zn} - Li_i pairs are highly probable to annihilate to form Li_{Zn} due to lower formation energy of Li_{Zn} with respect to Li_i .⁵⁴ Furthermore, $(\text{H}-\text{Li}_{\text{Zn}})^0$ can also form via Li_i occupying a V_{Zn} where an H or ^2H is already present. Hence, two additional reactions

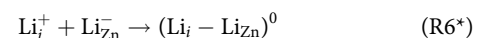


and



have been also included into the group of relevant ones.

On the other hand, reactions resulting in the formation of Li_{O} or Li_i - V_{O} complexes as well as of Li based molecules/trimers with H_i or OH have been excluded on the basis of theoretical results.^{54,60} Finally, the formation of the neutral Li_i - Li_{Zn} pair through the reaction



has also been theoretically found to be exothermic,⁵⁴ even though due to the presence of the competing processes, (R2) and (R6) are anticipated to have minor effect as verified independently and discussed hereafter. Simultaneous solution of the differential rate equations corresponding to the reactions (R1)–(R6) has been performed by (i) using the values listed in Table III for the diffusion coefficients and capture radii, (ii) setting $[\text{H}_i]/[^2\text{H}_i]$ and $[\text{Li}_{\text{Zn}}]$ initial values equal to the H/ ^2H implanted and $[\text{Li}]$ reported in Tables I and II, respectively, (iii) varying $[\text{Zn}_i]$ and $[\text{V}_{\text{Zn}}]$ in the 3%–6% range of the total amount created by ballistic collisions

according to TRIM simulations, (iv) assuming the concentrations of Li_i , H-Li_{Zn} , H-V_{Zn} and $\text{H}_2\text{-V}_{\text{Zn}}$ prior to the H or ^2H implantation negligible (equal to 10^{13} cm^{-3}) (v) keeping D_{Li_i} as a free parameter. D_{Li_i} has been determined by fitting the $[\text{Li}_i]$ extracted from the simulations, labeled as $[\text{Li}_i]^{\text{sim}}$ hereafter, with its experimental counterpart $[\Delta\text{Li}_i]^{\text{exp}}$. This approach is *a posteriori* justified by the time interval the reactions are occurring since $[\text{Li}_i]$ and $[\text{H-Li}_{\text{Zn}}]$ are reaching their equilibrium values ($\approx 10\%$ variation) in ≈ 3 h after the H or ^2H implantation. Secondly, it relies on the assumption that no additional reactions that can alter further $[\text{Li}_i]$ and $[\text{H-Li}_{\text{Zn}}]$ are occurring during the 200/400 °C annealing on the basis of the above discussion [see comment concerning (R1)].

The simulations clearly reproduce the dependence of $[\Delta\text{Li}_i]^{\text{exp}}$ on the different initial condition: $[\text{H}_i]/[^2\text{H}_i]$, $[\text{Li}_{\text{Zn}}]$, $[\text{Zn}_i]$, and $[\text{V}_{\text{Zn}}]$ as can be seen by looking at Fig. 3 where $[\Delta\text{Li}_i]^{\text{exp}}$ is compared with $[\text{Li}_i]^{\text{sim}}$ and plotted vs $\text{H}/^2\text{H}$ implanted concentration. Moreover, they confirm that in the case of D all the created Li_i is progressively going back to the Li_{Zn} configuration through (R5) due to the absence of H. In addition, the analysis indicates that Li not in the Li_i configuration is H or ^2H passivated with the highest $[\text{Li}_{\text{Zn}}]$ occurring in sample B, where it is found to be $\approx 10^{16} \text{ cm}^{-3}$ and its presence is caused by the limited amount of H introduced in this case. Furthermore, the reaction dynamics calculations prove that Li_i retrapping by V_{Zn} and H-V_{Zn} , i.e., (R5) and (R6), are crucial in determining the $[\text{Li}_i]$ to $[\text{H-Li}_{\text{Zn}}]$ ratio at high H or ^2H implantation levels, thus determining the $[\Delta\text{Li}_i]^{\text{exp}}$ drop observed when $[\text{H}]$ is $\approx 3 \times 10^{18} \text{ cm}^{-3}$. To investigate in more detail the (R5) and (R6) weight on the overall results, simulations excluding these two reactions and setting $[\text{Li}_{\text{Zn}}]$ equal to sample C concentration have been performed with the resulting $[\text{Li}_i]^{\text{sim}}$ reported as a dashed curve in Fig. 3. Consistent with the higher diffusion coefficient of

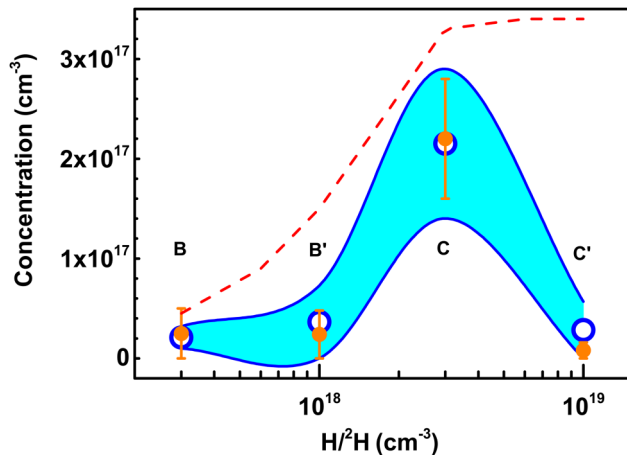


FIG. 3. Comparison between the simulated $[\text{Li}_i]^{\text{sim}}$ (cyan band) and measured $[\Delta\text{Li}_i]^{\text{exp}}$ (orange circles) vs H and ^2H implanted concentrations as extracted from SIMS measurements. The band outside of the simulated points is introduced to guide the eye only. The dashed red line indicates the dependence of $[\text{Li}_i]^{\text{sim}}$ on $[\text{H}]$ for sample C obtained by performing the simulations excluding reactions (R5) and (R6), i.e., assuming Li_i not mobile.

Zn_i with respect to H_i (R2) is not relevant at low H implanted concentration and $[\text{Li}_i]$ equals $[\text{Zn}_i]$. This proportionality breaks at $[\text{H}_i] \sim 3 \times 10^{18} \text{ cm}^{-3}$ after which $[\text{Li}_i]^{\text{sim}}$ is only slightly increasing and stabilizing at $\sim 3.4 \times 10^{17} \text{ cm}^{-3}$. Only $\sim 3 \times 10^{16} \text{ cm}^{-3}$ Li is H passivated in this case. On the other hand, as can be seen by comparing the dash line with $[\text{Li}_i]^{\text{sim}}$ for sample C, (R5) and (R6) account for a $\sim 10^{17} \text{ cm}^{-3}$ drop. Similarly it is mainly because of Li_i retrapping by V_{Zn} and H-V_{Zn} that H-Li_{Zn} is the dominant Li configuration in sample C where $[\text{H-Li}_{\text{Zn}}]$ equals to $\sim 10^{17} \text{ cm}^{-3}$. Indeed, as shown in Fig. 2(d), minor changes in the Li profile are observed after successive annealing up to 700 °C. This further supports the theoretical calculations, since $(\text{H-Li}_{\text{Zn}})$ is expected to be thermally stable up to ~ 1200 °C.⁶¹ Furthermore, this finding is in agreement with a recently published work, where, an almost identical Li profile obtained by H implantation, was found to be stable up to 800 °C and correlate with the H distribution.⁶² Finally, it is found that $[\text{Li}_{\text{Zn}}]$ spot dependence, extension of the $[\text{Zn}_i]/[\text{V}_{\text{Zn}}]$ range as well as the extracted D_{Li_i} optimal interval (hereafter discussed thoroughly) have a similar impact on the resulting $[\text{Li}_i]^{\text{sim}}$ introducing, each of them, variations similar to the uncertainties reported in Fig. 3 in exception of B where D_{Li_i} and $[\text{Zn}_i]/[\text{V}_{\text{Zn}}]$ ranges are the main sources of uncertainty.

The reaction analysis performed indicates that in ≈ 3 h after the implantation the initial $[\text{V}_{\text{Zn}}]$ has already been filled with two H or ^2H and $[\text{H-V}_{\text{Zn}}]$ is $\approx 3 \times 10^{15} \text{ cm}^{-3}$. $\text{H}_2\text{-V}_{\text{Zn}}$ are expected to be stable and/or to aggregate and form hydrogen filled bubbles after annealing up to 500 °C.²² On the other hand, as mentioned above, as H or ^2H implanted samples are highly resistive and a subsequent annealing at 200 °C has been found to be necessary for obtaining layers with optimal electrical characteristics.^{9,11,27} Then, the presented calculations suggest oxygen sublattice related defects as a source of compensating centers responsible for the observed postimplantation resistivity increase. Indeed, the reported theoretically calculated temperature for annealing out of primary defects situated in the oxygen sublattice by O_i^{2-} migration is ~ 170 °C, which is consistent with the annealing temperature experimentally found as well as the defect nature deduced here.⁵⁰

Concerning D_{Li_i} , the optimal range has been found to be $5 \times 10^{-16} - 3 \times 10^{-15} \text{ cm}^2 \text{ s}^{-1}$. This implies an activation energy for Li_i diffusion, $E_{\text{diff}}^{\text{Li}_i}$, equal to $(0.71 \pm 0.02) \text{ eV}$ if it is assumed that D_{Li_i} follows an Arrhenius form like $D_0 \exp(-E_{\text{diff}}^{\text{Li}_i}/k_B T)$ and a typical value of $10^{-3} \text{ cm}^2/\text{s}$ for the pre-exponential factor is used.⁶³ Even though there is overlapping between the $E_{\text{diff}}^{\text{Li}_i}$ found here and the theoretical predicted values, it is worth underlining that this estimate relies heavily on the value assumed for D_0 that might deviate significantly. Secondly, for sample C, it has been numerically verified that a $\sim 0.05 \text{ eV}$ higher $E_{\text{diff}}^{\text{Li}_i}$ has to be used to limit (R5) and (R6) action and achieve the same $[\text{Li}_i]^{\text{sim}}$ if $[\text{Li}]$ is reduced to 80% of the value reported in Table II. That is, possible presence of $[\text{Li}]$ already in the H-Li_{Zn} configuration or inactive because trapped at inversion domain boundaries, as discussed in Subsection IV B, might also affect to some degree the value of $E_{\text{diff}}^{\text{Li}_i}$. Hence, the estimate found here has to be considered as indicative.

Finally, simulations by successively adding to the (R1)–(R6) system of differential equations the contribution corresponding to (R4*), (R4**) (with $[\text{V}_\text{O}]$ equal to 6% of the total amount created by ballistic collisions according to TRIM simulations) and (R6*)

have been also performed. The largest correction has been found to take place in sample B, when (R6*) is included, with all the remaining ones being well within the error range shown in Fig. 3. In this case, as mentioned above, part of the Li_{Zn} is not H passivated and, therefore, contributes to the formation of $(\text{Li}_i\text{-Li}_{\text{Zn}})^0$ complexes. Because of this effect, $[\text{Li}_i]^{\text{sim}}$ is decreasing from $\sim 2 \times 10^{16} \text{ cm}^{-3}$ to $\sim 10^{16} \text{ cm}^{-3}$. Unfortunately, error ranges of $[\text{Li}_i]^{\text{sim}}$ as well as $[\Delta\text{Li}_i]^{\text{exp}}$ are too large for establishing if this correction is significative, i.e., (R6*) is actually taking place.

In conclusion, consequent to the $\text{H}/^2\text{H}$ implantation, the reaction simulation analysis evidences that Li_{Zn} up to a depth $d_{\text{Li lean}} \cong d_{\text{impl}}$ is mainly passivated with the formation of the H-Li_{Zn} complex and promoted to the Li_i position as a consequence of the Zn_i interstitialcy diffusion mechanism with the ratio between the two configurations depending on the details of the H, Li, Zn_i , and V_{Zn} interplay. The purpose of Subsections IV B and IV C is to provide additional experimental evidence of the proposed scenario.

B. Electrical properties

In Fig. 4(a) $n(T)$ and in (b) $\mu(T)$ for the reference samples A and A' are shown. In this figure, $n_{\text{imp}}(T)$ and $\mu_{\text{imp}}(T)$ for B, as extracted from the multilayer analysis, are also included. Results concerning samples B', C, and C' are presented in Figs. 5(a) and 5(b) instead. As a consequence of H or ^2H implantation, $n(T)$ is seen to increase from a RT value of $\sim 10^{14} \text{ cm}^{-3}$ to $\sim 2 \times 10^{17} \text{ cm}^{-3}$ and from $\sim 2 \times 10^{13} \text{ cm}^{-3}$ to $\sim 8 \times 10^{16} \text{ cm}^{-3}$ in the A-C and A'-C' series, respectively. Secondly, the $n(T)$ profiles have been found to flatten down when H or ^2H is introduced, thus suggesting the presence of donors with lower activation energies in these cases.

An analog dramatic change has been also observed to occur in $\mu(T)$ consequent to the H or ^2H introduction. In detail, the mobility from a starting value of $\sim 130 \text{ cm}^2 \text{ V}^{-1} \text{ s}^{-1}$ is raising up to $\sim 540 \text{ cm}^2 \text{ V}^{-1} \text{ s}^{-1}$ with the temperature peak shifting from $\sim 200 \text{ K}$ down to $\sim 70 \text{ K}$, if measurements on A and C are compared. An even larger peak mobility increase up to $\sim 1200 \text{ cm}^2 \text{ V}^{-1} \text{ s}^{-1}$ is observed in the case of samples B' and C'.

The simulated curves are also included in Figs. 4 and 5. As can be seen, good agreement between the experimental data and the simulations has been achieved. The main incongruity is a substantial discrepancy of the modeled $n(T)_{\text{imp}}$ observed for temperatures $\leq 40 \text{ K}$ in the case of samples C, B', and C' with the temperature range pointing to the surface layer contribution as main cause. The parameters extracted from the fits are listed in Table IV. In detail, the references A and A', where $[\text{Li}] > [\text{Al}] + [\text{Ga}]$ (see Table II), are found to be similar to previously examined high resistive samples.³⁰ That is, D_2 is fully compensated and the conduction band free carriers are provided by the deep donor D_3 with $E_{D_3} \sim 320 \text{ meV}$ corresponding to the electrically active defect labeled as E_3 , whose presence is commonly reported in HT-ZnO .^{35,64-66} Here, it is also worth noticing that, in principle, the TDH measurements of these samples can be simulated assuming that only N_{D_2} and N_{D_3} are present. However, considering that N_{D_2} is fixed, by being set equal to $([\text{Al}] + [\text{Ga}])$, from the combined fit of $n(T)$ and $\mu(T)$, the presence of a third donor cannot be excluded *a priori*. On this basis, an upper limit for N_{D_1} concentration has been established

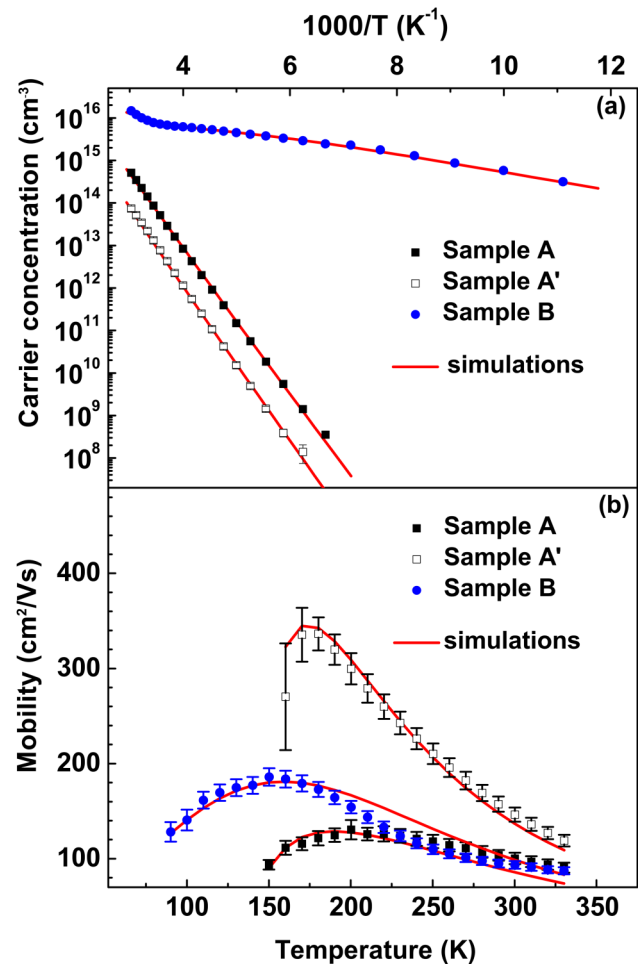


FIG. 4. (a) $n(T)$, the carrier concentration vs temperature, for the reference samples A and A' and $n_{\text{imp}}(T)$ for sample B. (b) $\mu(T)$, the mobility vs temperature, for the reference samples A and A' and $\mu_{\text{imp}}(T)$ for sample B. The solid curves are fit to the experimental data.

(see Table IV), even though no activation energy can be evaluated in these cases since the shallow donors are fully compensated.

In all the H or ^2H implanted samples, the evidence for the presence of two shallower and electrically active donors, D_1 and D_2 , has been clearly found with activation energies varying in the $\sim 20\text{--}55 \text{ meV}$ range. To compare the activation energies among them and with the ones extracted from the PL measurements presented in Subsection IV C, the infinite dilution values of E_{D_1} and E_{D_2} , indicated in Table IV as $E_{D_1}^0$ and $E_{D_2}^0$, respectively, have been calculated as⁶⁷

$$E_{D_i}^0 = E_{D_i} + \beta \sqrt[3]{N_A^-}, \quad (4)$$

with $\beta = 4 \times 10^{-5} \text{ meV cm}$ as theoretically predicted. Concerning β , here it is worth pointing out that available experimental estimates are varying in the $\sim 2\text{--}6 \times 10^{-5} \text{ meV cm}$ range depending on

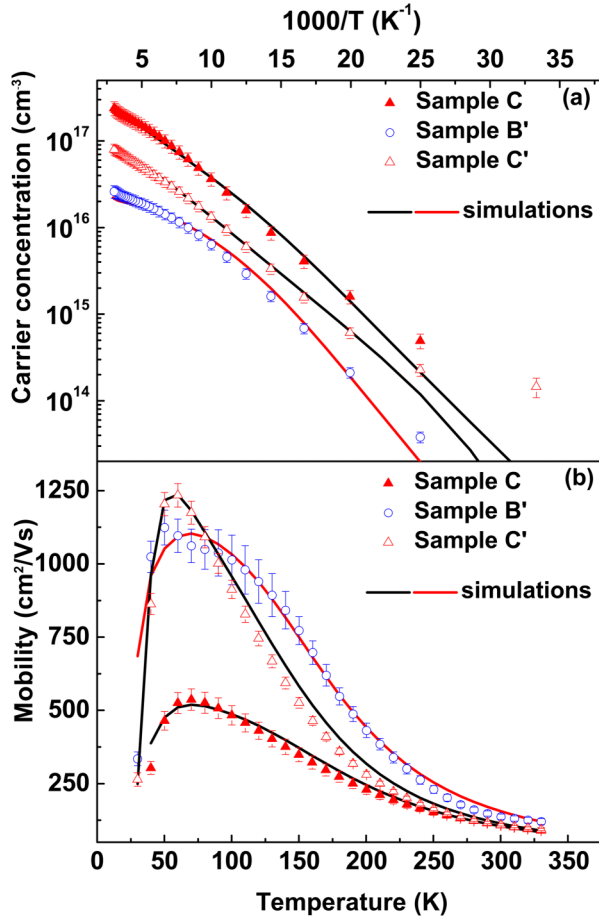


FIG. 5. (a) $n_{imp}(T)$ for samples C, B', and C'. (b) The corresponding $\mu_{imp}(T)$. In both cases, the fit to the experimental data is drawn as solid curves.

the semiconductor.⁶⁸ Hence, using in Eq. (4), the experimental values span instead would cause an increase in the E_{D1}^0 and E_{D2}^0 uncertainties, while the resulting means are remaining within the interval reported in Table IV.

TABLE IV. Extracted parameters from fitting the TDH measurements. Activation energies, E_{Di} ($i = 1, 2, 3$), and their infinite dilution limit, E_{Di}^0 ($i = 1, 2$), are in meV. Donor concentrations, N_{D1} and N_{D3} , ionized compensating acceptors concentration, N_A^- , are in 10^{16} cm^{-3} , longitudinal optical phonon energies, $\hbar\omega_{op}^H$, are in meV, and the space-charge effective linear dimensions, R_{SC} , are in nm.

| | N_{D1} | E_{D1} | E_{D1}^0 | E_{D2} | E_{D2}^0 | N_{D3} | E_{D3} | N_A^- | $\hbar\omega_{op}^H$ ^a | R_{SC} |
|----|---------------|------------|------------|-------------|-------------|------------|--------------|---------------|-----------------------------------|--------------|
| A | ≤ 0.5 | | | | | 11 ± 3 | 318 ± 3 | 32 ± 1 | 71 | ≥ 1000 |
| B | 2 ± 1 | ~ 20 | ~ 40 | 31 ± 1 | 53 ± 2 | 10 ± 6 | 220 ± 20 | 16 ± 1 | 71 | ≥ 400 |
| C | 17 ± 3 | 27 ± 1 | 38 ± 2 | 49 ± 7 | 60 ± 10 | ≤ 5 | | 2 ± 1 | 67 ± 3 | 80 ± 20 |
| A' | ≤ 0.6 | | | | | 20 ± 5 | 333 ± 2 | 6 ± 1 | 71 | ≥ 1000 |
| B' | 2.2 ± 0.3 | 34 ± 1 | 41 ± 3 | 55 ± 10 | 60 ± 10 | 9 ± 3 | | 0.5 ± 0.3 | 71 | ≥ 1000 |
| C' | 7.7 ± 0.3 | 45 ± 2 | 47 ± 4 | | | 3 ± 2 | | ≤ 0.04 | 65 ± 2 | 250 ± 50 |

^a $\hbar\omega_{op}^H$ has been extracted from the $\mu_{imp}(T)$ fitting only in the case of samples C and C' as discussed in detail in the text.

Once the infinite dilution correction is performed, agreement for E_{D2} is found among the samples.⁶⁹ Furthermore, the extracted E_{D2}^0 is consistent with setting N_{D2} equal to $([Al]+[Ga])$ since Al_{Zn} and Ga_{Zn} related levels are reported to occur in the $\sim 52\text{--}55$ meV range on the basis of PL measurements.^{8,44} Hence, within the approach used, these findings suggest that Al and the combination of Al and Ga are the major contributors to the level with E_{D2}^0 in the 53–60 meV range in the series of samples A-C and A'-C', respectively. That is, other possible donor candidates, like residual H_{BC} or transition metal stabilized H related donors, $TM_{Zn}\text{-}H_{BC}$,¹⁵ appear to play a minor role similarly to that reported for analogous samples.³⁴ Moreover, the occurrence in samples B, C, and B' of the second shallow donor with $E_{D1}^0 \sim 40$ meV is consistent with the presence of Li_i since there is theoretical and experimental consensus that Li_i is providing a shallow donor with a reported activation energy equal to ~ 44 meV.^{3,51,54,59} Furthermore, the proposed scenario based on the reaction dynamics results is further corroborated by the fact that in C', where $[\Delta Li_i]^{exp} \leq 10^{16} \text{ cm}^{-3}$ (limiting the analysis to the 0.4–2.4 μm range), E_{D1}^0 is found to be ~ 7 meV higher than in the remaining samples, thus supporting the involvement of a different donor in the latter case. Finally, in the H and ²H implanted samples, direct evidence for the presence of a deep donor has been found only in B. This contribution has been assumed in the following discussions to be E_3 related despite the ~ 0.1 eV lower E_{D3} . Both the limited temperature interval where D_3 is significantly ionized as well as the large substrate correction (see Appendix) are, possibly, responsible for the ~ 0.1 eV shallower E_{D3} extracted in this case. On the other hand, in the remaining ones, C, B', and C', the presence of the shallower and electrically active donors, D_1 and D_2 , mask the possible contribution of D_3 to $n_{imp}(T)$ in the temperature range analyzed here. Therefore, N_{D3} has been evaluated exclusively on the basis of its contribution to the neutral impurity scattering, a procedure that has been verified to provide results in substantial agreement with those extracted from TAS measurements.^{30,35} The comparison with samples A and A' strongly supports to assign N_{D3} to E_3 also in these cases. Hence, N_{D3} decrease observed in samples C, B', and C' suggests H and ²H passivation of the defect responsible for the E_3 level, conclusion also in agreement with recently published results.⁷⁰

As anticipated by the dramatic increase in $\mu_{imp}(T)$, a N_A^- reduction of ~ 1 and ~ 2 orders of magnitude is observed in the case of samples C/B' and C', respectively (see Table IV).

This points to a passivation of the acceptors present with the ~ 2 orders of magnitude lower $[Al]$ of B' and C' playing a distinct role in the $\sim 600 \text{ cm}^2 \text{ V}^{-1} \text{ s}^{-1}$ higher mobility maximum compared to that of sample C . The results found here are in accordance with the above proposed scenario since, as mentioned, Li_{Zn} is expected to be the main compensating center and the formation of $(H-Li_{Zn})^0$ complexes following the H or 2H implantation is causing the N_A^- reduction. This interpretation is further corroborated by observing that similar increases in peak mobility have been reported in HT -ZnO samples with a $[Li]$ reduced to $\sim 10^{15} \text{ cm}^{-3}$ as a consequence of high temperature annealing.³⁴ Moreover, it is worth pointing out that N_A^- for sample A and A' are $\sim 80\%$ and $\sim 40\%$, respectively, of the total $[Li]$ measured by SIMS in the respective samples. However, as evident from Table II, large variation in $[Li]$ has been observed between the samples belonging to the same wafer and there is an overlap between N_A^- and the overall Li concentration range occurring within the wafer. Therefore, it is not possible to establish if the above mentioned discrepancy is related to $[Li]$ fluctuations or to a non-negligible presence of $(H-Li_{Zn})^0$ and/or Li trapped at inversion domain boundaries, as an example.⁴⁷ Finally, it should be noted that in the high $H/^2H$ concentrations implanted samples, i.e., C , B' and C' , Li_{Zn} is expected to be fully passivated according to the reaction dynamics simulations discussed in Subsection IV A, while N_A^- is found $\leq 2 \times 10^{16} \text{ cm}^{-3}$. The presence of additional compensating centers³⁰ and/or corrections due to contributions of slower reactions occurring already at RT and not included in the analysis presented in Subsection IV A are all factors that can contribute, for example, to this deviation from the main trends of the proposed scenario.

An upper bound for R_{SC} varying in the 400–1000 nm range could be evaluated in samples A , A' , and B with the extracted values listed in Table IV. In these cases, the estimates represent the threshold where, by decreasing R_{SC} further, the simulated $\mu_{imp}(T)$ curve was pushed below the experimental errors. That is, no clear experimental evidence for the presence of this scattering mechanism in the as-grown material has been found contrary to what has been previously reported.⁷¹ On the other hand, for samples C and C' , a distinct improvement in the $\mu_{imp}(T)$ fit has been found by introducing the SC scattering contribution, thus permitting an accurate evaluation of R_{SC} . This suggests that higher H or 2H implanted doses can introduce defects contributing to the space-charge scattering. As mentioned in Sec. I, the formation of H-filled bubbles upon annealing up to 500°C in H implanted samples has been observed by PAS and their presence is consistent with theoretical calculation showing that significant V_{Zn} clustering with V_O is starting at temperatures $\geq 100^\circ\text{C}$.^{21,22} Considering that the 2H total dose in the case of sample C' is only a factor ~ 2 lower than in the above mentioned experimental study, the presence of vacancy clusters is anticipated in our samples and represent an evident candidate for the observed increase in the SC contribution. Then, if σ_{SC} is assumed to be equal to $\sim 2\text{--}30 \text{ nm}$ corresponding to the vacancy cluster diameter observed by transmission electron microscopy in a study on H implanted ZnO samples, a geometrical averaged N_{SC} equal to $\sim 10^{17} \text{ cm}^{-3}$ is estimated for both samples. In addition, in the case of C and C' , for achieving good agreement between the measured data and simulated curves, it has been found necessary to lower the longitudinal optical (LO) phonon

energy, $\hbar\omega_{op}^H$, from the assumed value of 71 meV to $\sim 67 \text{ meV}$ and $\sim 65 \text{ meV}$, respectively. The presence of a broad band ranging from $\sim 62 \text{ meV}$ to $\sim 74 \text{ meV}$ around the LO mode has been observed in Raman spectra of ZnO samples implanted with Ar and H. This phenomenon has been attributed to the weakening of the crystal translational invariance that is making possible the scattering contribution from outside the Brillouin zone center. This interpretation is supporting the use of a lower $\hbar\omega_{op}^H$ in the samples implanted with the highest H or 2H doses.^{22,72} Finally, $\mu_{imp}(T)$ simulations indicate that N_{dis} increases from the typical value of $\sim 10^4\text{--}10^5 \text{ cm}^{-2}$ of the reference samples^{30,73} to $\geq 10^6 \text{ cm}^{-2}$ in samples C and C' . However, the scattering dislocation contribution becomes relevant only below $\sim 50 \text{ K}$. Hence, the above mentioned N_{dis} increase appears to be strongly correlated with the surface layer correction (see Appendix). Therefore, the values extracted can be only taken as indicative and are not reported in Table IV.

A comparison between the He implanted and reference sample electrical characteristics, i.e., samples D and A , is shown in Fig. 6. As a consequence of He implantation, μ_H^T and n_H^T have been observed to scatter around sample A values. This suggests the presence of a high resistivity layer. In addition, large asymmetries in the measured Hall coefficient by ramping the magnetic field at both negative and positive direction were present for measurements taken at temperatures $>280 \text{ K}$ that are, therefore, not

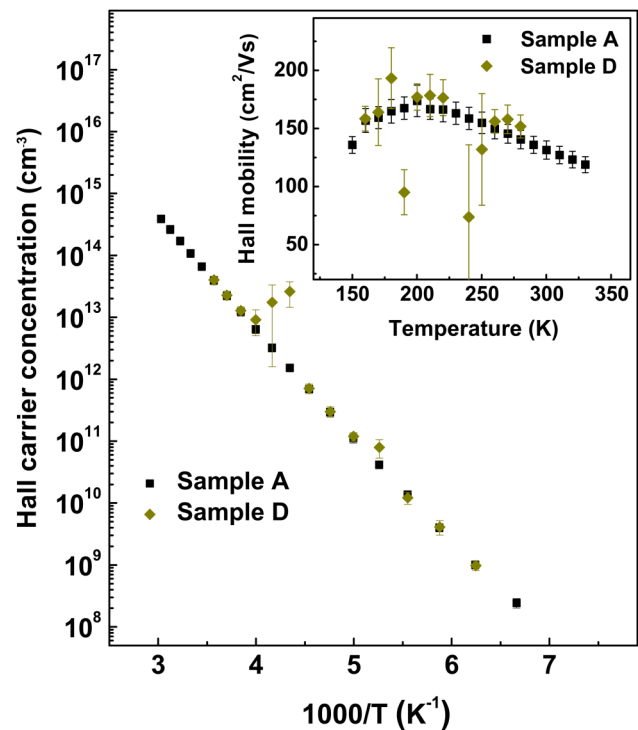


FIG. 6. Samples A and D Hall carrier concentration and Hall mobility data (in the inset) as measured, i.e., assuming an uniform thick layer equal to the wafers nominal thickness.

shown in Fig. 6. A detailed study on the onset of RT Hall coefficient asymmetries is beyond the purpose of the present report and will not be discussed further.

Assuming an extension of the He implanted layer of $(1.5 \pm 0.2)\mu\text{m}$, as obtained from TRIM simulations, an order of magnitude for ρ_{He} can be evaluated by noticing that if $\rho_{\text{He}} \gg \rho_j$ then $\mu_{\text{H}}^{T2} n_{\text{H}}^T d_T = \mu_{\text{H}}^{i2} n_{\text{H}}^i d_i + \mu_{\text{H}}^{j2} n_{\text{H}}^j d_j t^2$ obtained by combining Eqs. (A1) and (A2) reduces to

$$t \sim \sqrt{\frac{\mu_{\text{H}}^{T2} n_{\text{H}}^T d_T}{\mu_{\text{H}}^{j2} n_{\text{H}}^j d_j}}. \quad (5)$$

Following this approach by using Eq. (A3), it is found that ρ_{He} is $\sim 10 \cdot \rho_A$, thus justifying *a posteriori* the simplifying assumption made. Starting from the carrier concentration simulations of sample A, an acceptor concentration increment, ΔN_A^- , of $\lesssim 10^{17} \text{ cm}^{-3}$ corresponds to such a resistivity increase. That is, the 200°C annealing is not sufficient for a full recovery of the material to the original condition in case of He implantation. This is indeed expected considering the absence of V_{Zn} passivation by H (see also Subsection IV A) and suggests the presence of residual V_{Zn} as a cause for the ΔN_A^- , in agreement with already published results.⁷⁴

In conclusion, comparison of the electrical characteristics of sample D with the remaining ones excludes that the dramatic changes in $n_{\text{imp}}(T)$ and $\mu_{\text{imp}}(T)$ observed in B, C, B', and C' are consequence of pure damaging produced by the implantation and confirms that H is playing a clear role in the results above discussed.

C. Near band edge emission characteristics

A comparison between the spectra taken inside a crater exposing a virgin region $\sim 5\text{--}6\mu\text{m}$ deep into the B/C and B'/C' samples with the ones taken on the surface of A and A' is shown in Figs. 7(a) and 7(b), respectively. It can be seen that only minor changes in the near band edge (NBE) spectra features are observed as a consequence of the sputtering to realize the craters, thus justifying the procedure used here. The dominating peak labeled as DX and occurring at $\sim 3.361 \text{ eV}$ is in the energy range of the neutral donor bound excitons region⁴⁴ and has been found to be present in all the samples. Three other peaks are clearly visible in the spectra of the references and virgin region of the samples. Considering their localizations they are indicated in Figs. 7(a) and 7(b) as D^+X , DX-TES and DX-LO, respectively. In the case of sample A, as reported in Table V, agreement is found between E_{DX}^{H} and $E_{\text{DX}}^{\text{TES}}$ with both estimates equal to $\sim 51 \text{ meV}$. The presence of a level with this position in the bandgap is anticipated by the results discussed in Subsection IV B and is consistent with attributing D_2 mainly to Al, since lines in the $3.3608\text{--}3.3604 \text{ eV}$ range (I_6/I_{6a} in the literature) are commonly assigned to excitons bound to neutral Al_{Zn} donors.⁴⁴ Here, it is worth pointing out that the intrinsic FWHM width of the DX peaks is $\sim 1\text{--}2 \text{ meV}$. Hence, other defects, like residual H_{BC} , Ga_{Zn} as well as the unassigned I_5 and I_7 lines, that are all reported to occur within $< 2 \text{ meV}$, might also participate to DX. However, the occurrence of the D^+X peak with localization energy $\sim 3 \text{ meV}$ and attributed to excitons bound to ionized Al_{Zn} points unambiguously to a I_6/I_{6a} contribution to the DX signal.⁴⁴ Finally, it has been verified that the energy distance between DX and DX-LO is

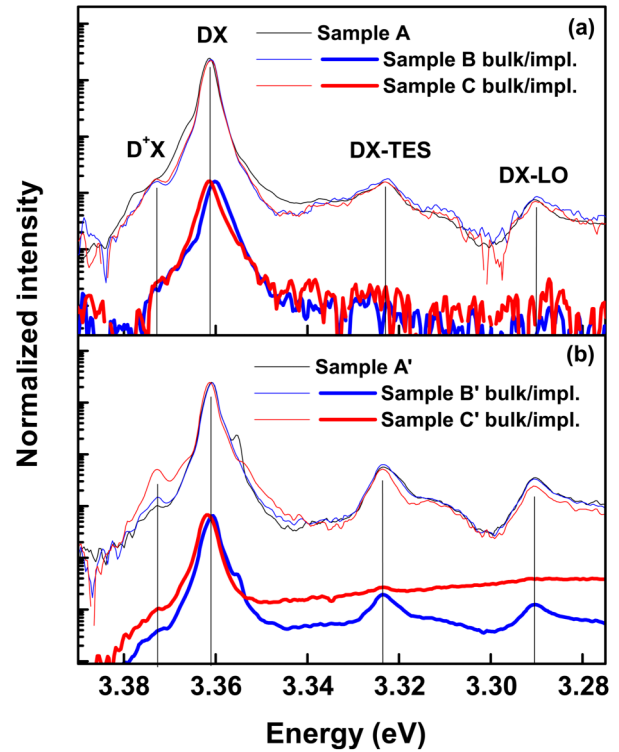


FIG. 7. Normalized PL spectra for the A-C and for the A'-C' series are shown in (a) and (b), respectively. For each of the implanted samples, two spectra are shown. They are labeled as "bulk" and "implanted" to indicate the spectra collected from craters $\sim 5\text{--}6\mu\text{m}$ and $\sim 1.6\text{--}2.4\mu\text{m}$ deep, respectively. The bulk spectra are compared with the ones taken on the surface of samples A/A' in the upper part of each subfigure. D^+X , DX, DX-LO, and TES denote exciton bound to ionized donor, to neutral donor, the corresponding phonon replica and two electron satellite related lines, respectively.

$\sim 71 \text{ meV}$ in full agreement with the $\hbar\omega_{\text{op}}^{\text{H}}$ used in the TDH measurement simulations (excluding the case of samples C and C').

The values extracted in the bulk region of samples B and C are in agreement with those of A; hence, they are not discussed or

TABLE V. DX binding energy obtained from "Haynes" rule, E_{DX}^{H} and from the DX-TES energy distance, $E_{\text{DX}}^{\text{TES}}$. The longitudinal optical phonon energy $\hbar\omega_{\text{op}}^{\text{PL}}$ equal to $E_{\text{DX}^+} - E_{\text{DX-LO}}$ is also reported. All values are in meV.

| | E_{DX}^{H} | $E_{\text{DX}}^{\text{TES}}$ | $\hbar\omega_{\text{op}}^{\text{PL}}$ |
|----|----------------------------|------------------------------|---------------------------------------|
| A | (51 ± 1) | (51 ± 1) | (71 ± 1) |
| B | (53 ± 1) | | |
| C | (50 ± 1) | | |
| A' | (51 ± 1) | (51 ± 1) | (71 ± 1) |
| B' | (51 ± 2) | (50 ± 1) | (70 ± 1) |
| C' | (49 ± 1) | | |
| | $(51 \pm 1)^{\text{a}}$ | | |
| | $\sim 53^{\text{a}}$ | | |

^aValues extracted from high resolution PL spectra only.

reported in Table V. In general, an overall post-H implantation reduction of the PL signal has been observed. Furthermore, in this case D^+X , DX -TES and DX -LO related peaks are not distinguishable as can be seen by looking at the spectra shown in the lower part of Fig. 7(a). This might be related to the weakening of the crystal translational invariance caused by the implantation damage discussed in Sec. IV B. On the other hand, in the case of D^+X , Li_{Zn} passivation, subsequent to the H or ^2H implantation, implies a compensation reduction and correspondingly a lower concentration of fully ionized Al_{Zn} donors at the temperature where the PL spectra are acquired. Therefore, this effect may also contribute to the reduction of the D^+X peak intensity. In addition, DX in sample C appears to occur within the range of values observed in the case of A, while a ~ 1 meV redshift has been observed in the case of B. High resolution PL measurements on the A-C series surfaces shown in Fig. 8(a) confirmed the presence of a ~ 0.8 meV deviation vs lower energies in this case. The E_{DX}^H values, as extracted from the spectra shown in Figs. 7(a) and 8(a) for both sample B and C, are reported in Table V with the errors indicating the variation between the two measurements. It can be seen that a ~ 2 meV higher E_{DX}^H corresponds to the above mentioned DX line shift in sample B. The exact physical mechanisms behind the higher E_{DX}^H observed in this case cannot be unambiguously addressed within the present analysis, even though an interplay between the above mentioned I_6/I_{6a} lines seems plausible on the basis of published results.^{44,75} The same analysis was conducted on the A'-C' series and the corresponding results are also summarized in Table V. Values extracted from the measurements performed on A' as well as on the virgin region ~ 5 - $6 \mu\text{m}$ deep into samples B' and C' (not included in Table V) are similar to the A-C case and the results can be analogously interpreted. Concerning the spectra taken $\sim 2.4 \mu\text{m}$ deep into the implanted region, TES and DX -LO transitions are still clearly visible also in the case of B', with indication of their presence being found also in C'. In the case of B', the values for E_{DX}^H , E_{DX}^{TES} , and $\hbar\omega_{\text{op}}^{\text{PL}}$ extracted are in agreement with what found in the remaining samples, while for sample C' a ~ 1 meV

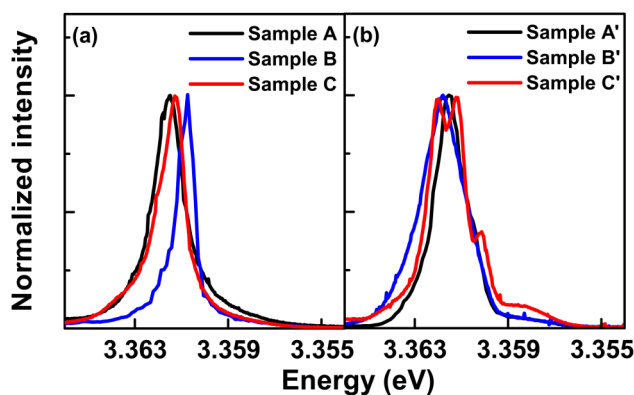


FIG. 8. High resolution PL spectra normalized to the DX intensity for all the H (a) and ^2H implanted samples (b) and their respective references. All spectra have been measured on the sample surface in this case.

lower activation energy is obtained due to an unambiguous shift of the main peak towards lower localization energies. The presence of three closely spaced lines with corresponding E_{DX}^H equal to (49 ± 1) , (51 ± 1) and ~ 53 meV has been observed in high resolution PL measurements performed on the surface of C' as shown in Fig. 8(b). The latter values are, as mentioned above, consistent with being related to excitons bound to neutral Al_{Zn} , i.e., to I_6 and I_{6a} lines, while the former is in agreement with the E_{D1}^0 value extracted from the TDH measurements. Here, it is not possible to establish the nature of the defect involved in the latter recombination on the basis of already published results since it appears to be located between the I_4 line position assigned to H_0 and peaks ~ 1 meV lower in energy that have been attributed to H_3 - V_{Zn} or H_4 - V_{Zn} complexes.^{11,44,76,77} Considering that C' is the sample with the highest ^2H implanted concentration, these findings suggest that damage and/or line broadening caused by the implantation are not the main reasons for the absence of the D_1 related peak in the remaining samples. On the contrary, this points to other causes like low N_{D1} or the different nature of the defect responsible for the D_1 level as possible reasons for its nonappearance in B, C, and B'. The latter hypothesis appears as more probable in light not only of the results discussed in Subsections IV A and IV B, but also since Li indiffusion has been reported not to introduce any new neutral donor bound exciton line.⁷⁸ Furthermore, emerging of a broad shoulder at ~ 3.358 meV has been observed in C' [see Fig. 8(b)]. This additional signature is energetically located between the expected position of the I_{8a} and I_9 lines⁴⁴ and corresponds to an activation energy of ~ 58 meV. Considering that this value falls into the E_{D2}^0 range extracted from TDH measurements (cf. Table IV) the concentration of the donor/s involved is limited to the $([\text{Al}] + [\text{Ga}])$ uncertainty (cf. Table II). However, the impossibility to clearly resolve the peak position, its intrinsic width as well as the lack of additional signatures prevent a clear assignment. Finally, as shown in Fig. 7(b), an additional peak at ~ 3.355 meV has been also observed on the surface of sample A' and in the implanted region of sample B' with indication of its presence found also in the bulk region of C', while not evident in other cases [see also Fig. 8(b) where this peak is completely absent] as well as in the A-C series. Since its localization energy corresponds to $E_{DX}^H \sim 66$ meV, i.e., close to ~ 63 meV assigned to In ,⁴⁴ we attribute it to the residual In content present in the samples (see also Table II).

D. Li contribution to the D_1 level

As thoroughly discussed in Subsections IV B and IV C, the results extracted from the TDH and NBE-PL measurements besides being consistent with each other fit within the proposed scenario based on the reaction analysis. Then, on the basis of what is presented above, it is possible to quantify the Li_i contribution to N_{D1} . For taking into account Li_i redistribution already occurring after the 200°C annealing evident in the case of samples C and B' [see Figs. 2(c) and 2(b)], the difference between $[\text{Li}]$ prior and after the 400°C annealing averaged over $d_{\text{Li lean}}$, labeled as $[\text{Li}_i]$ hereafter, has been evaluated (excluding the first ~ 200 - 600 nm where, depending on the sample, Li piling up is observed). Afterward, the difference between $[\text{Li}_i]$ and ΔN_{D1} , obtained by subtracting the D_1 concentrations in the references A and A' from N_{D1} of B/C and B'/C'

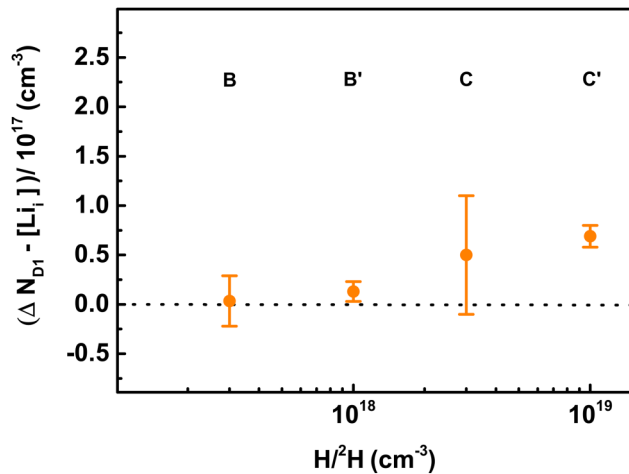


FIG. 9. Difference between ΔN_{D1} and $[Li_i]$ vs the H or ^2H concentration introduced by implantation. The dashed line is drawn to indicate the zero only.

respectively, has been computed. The obtained values are plotted in Fig. 9 against the H^2/H concentration introduced by implantation. It is found, on the basis of this comparison, that if the H or ^2H implanted concentration is $\lesssim 3 \times 10^{18} \text{ cm}^{-3}$ Li_i donor activity is contributing to ΔN_{D1} $\sim 70\%$ – 80% and $\sim 30\%$ in case of samples B/C and B', respectively. Furthermore, by looking at Fig. 9, it can be seen that, even though up to sample C, the measured $[Li_i]$ can account for ΔN_{D1} , the data points are progressively upshifting. This suggests the presence of one or more additional donors besides Li_i with close activation energy that are increasingly contributing to ΔN_{D1} .

As mentioned above, on the basis of the investigation performed, it is not possible to attribute firmly this additional contribution to H_O even though in sample C' where $[Li_i]$ is negligible E_{D1}^0 and E_{DX}^H as extracted from TDH and PL measurements, respectively, would be in good agreement with this assignment. However, even by assigning the residual ΔN_{D1} exclusively to H_O , the results presented in Fig. 9 indicate that the H^2/H percentage acting as a donor is in the $\sim 1\%$ – 2% range. This value is up to 2 orders of magnitude lower with respect to previous studies performed on samples originating from the same vendor as series A–D and implanted with $[H]$ up to $\sim 3 \times 10^{18} \text{ cm}^{-3}$.^{9,11} Finally, here it is worth underlining that the annealing dependence of the extracted shallow donor concentrations presented in the same studies can also be easily explained in light of the present results. That is, a $\sim 1 - 3 \times 10^{17} \text{ cm}^{-3}$ reduction in the concentration of donors with activation energy in the ~ 28 – 46 meV range has been observed after an annealing at 400°C . This decrease was attributed to a H reduced donor formation or H effusion, while, in the light of the results presented here, this effect appears to be, at least partly, most probably related to the Li_i out-diffusion from the implanted region as shown in Fig. 2 and thoroughly discussed above.

V. CONCLUSIONS

In this work, an alternative scenario concerning the effect of H or ^2H implantation in $HT\text{-ZnO}$ is proposed. In detail, it is shown

that in hydrogen implanted $HT\text{-ZnO}$, the assignment of defect levels presenting an activation energy of $\sim 40 \text{ meV}$ and $\sim 50 \text{ meV}$ to the two hydrogen related configurations H_O and H_{BC} , respectively, has to be done with care since Al and Li are present. In detail, the diffusion of Zn_is displaced during the H implantation creates Li_i that can contribute to a carrier concentration increase of $\sim 10^{17} \text{ cm}^{-3}$ by providing a donor level with activation energy (40 ± 4) meV and thus is very close to the value of $\sim 47 \text{ meV}$ expected for H_O . The Li_i amount introduced decreases with the implanted H doses due to Li_i retrapping by V_{Zn} and $H\text{-}V_{Zn}$ defects. Therefore, when $Li_{Zn} \sim 10^{17} \text{ cm}^{-3}$, H concentrations $> 3 \times 10^{18} \text{ cm}^{-3}$ have to be implanted to minimize this effect and possibly achieve H_O doping, even though no firm evidence of H_O formation has been found here. On the other hand, Al is providing a donor level that is energetically very close to the H_{BC} one. However, its presence might be electrically fully masked by the presence of Li_{Zn} that is passivating it. Following the H or ^2H implantation, it is again providing carriers to the conduction band due to the formation of neutral $H\text{-}Li_{Zn}$ complexes and, therefore, removal of compensation.

ACKNOWLEDGMENTS

R.S. is profoundly indebted to Professor B. G. Svensson for his inspiring support and discussions throughout the realization of the work presented here; unfortunately, he left before the manuscript was concluded and sent to the co-authors. Furthermore, the authors are grateful to V. Bobal (Department of Physics/Center for Material Science and Nanotechnology, University of Oslo, Oslo, Norway) and A. Hallén (Ion Technology Centre, Uppsala, Sweden) for the implantations. This work has been performed within the Polish National Science Centre (NCN) (Project No. UMO-2016/22/E/ST3/00553). Support from “The Norwegian Research Centre for Solar Cell Technology” (Project No. 193829) cosponsored by the Norwegian Research Council and research and industry partners in Norway, the Frienergi program, the NorFab (Project No. 245963), and the EU 7th Framework Programme (Project No. REGPOT-CT-2013-316014) (EAgLE) is also acknowledged.

APPENDIX: EXTRACTION OF THE H^2/H IMPLANTED LAYER CONTRIBUTION

The measured Hall mobility, μ_H^T , and Hall carrier concentration, n_H^T , corrected for the contact size effect⁷⁹ and evaluated using the wafers nominal thickness, d_T , equal to $(500 \pm 50) \mu\text{m}$ are shown in Fig. 10 for samples A, B, C and A', B', C'. Measurements taken below the displayed temperature exhibited clear asymmetries depending on the magnetic field direction; hence, they are neither shown nor discussed hereafter. In the present study, the extended multilayer model for top surface placed contacts has been used to extract the contribution of the H or ^2H implanted layer to the Hall measurements.⁸⁰ In the case of a two layer structure in this approach, μ_H^T and n_H^T are related to the contributions from the layers i and j according to the following equations:

$$\mu_H^T = \frac{\mu_H^{i2} n_H^i d_i + \mu_H^{j2} n_H^j d_j t^2}{\mu_H^i n_H^i d_i + \mu_H^j n_H^j d_j t} \quad (\text{A1})$$

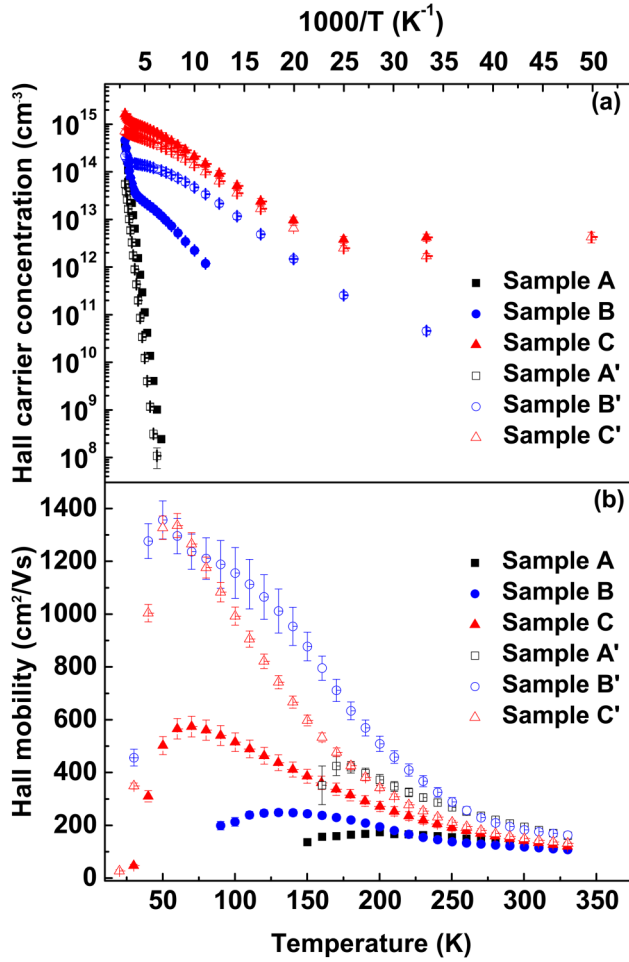


FIG. 10. Hall carrier concentration (a) and Hall mobility (b) of samples A, B, C and A', B', C' corrected for the contact size assuming an uniform $(500 \pm 50) \mu\text{m}$ thick layer equal to the wafers nominal thickness.

$$n_H^T = \frac{1}{d_T} \frac{(\mu_H^i n_H^i d_i + \mu_H^j n_H^j d_j t)^2}{\mu_H^{i2} n_H^i d_i + \mu_H^{j2} n_H^j d_j t^2}, \quad (\text{A2})$$

$$t = \frac{1}{1 + \frac{\mu_H^i n_H^i 2d_i d_j}{\mu_H^j n_H^j S}}, \quad (\text{A3})$$

where μ_H^i , n_H^i , d_i , and μ_H^j , n_H^j , d_j are the Hall mobility, Hall carrier concentration, and layer thickness of the upper layer i and lower lying layer j , respectively. The analysis employed here differs from the ordinary multilayer analysis employed in other cases (see, for example, Ref. 71) for the presence of t . This correction factor accounts for the fact that two layers i and j are only partially connected in parallel to each other through the areas lying below the contacts that are assumed to have a surface extension equal to S . Here, it is also worth mentioning that such an analysis based on

Eqs. (A1)–(A3) is not limited to the two layer case. That is, in the case of a multilayered structure by iterating the two layer approach, the electrical properties of the layer of interest can be extracted if, besides the overall Hall carrier concentration and mobility, the electrical parameters of the remaining ones are also known independently.

1. Surface layer contribution

Surface layer conductivity has been shown to be present in commercially available as received^{81–84} as well as annealed ZnO wafers.^{28,85,86} Furthermore, it has been shown by using variable field magnetotransport measurements that the surface layer might play a major role in lowering the mobility peak from $\sim 1100 \text{ cm}^2 \text{ V}^{-1} \text{ s}^{-1}$ down to $\sim 400 \text{ cm}^2 \text{ V}^{-1} \text{ s}^{-1}$ when TDH measurements are performed on highly compensated ZnO.⁸²

In our study, experimental evidence for the presence of residual surface conduction has been found only in C and C', as can be seen in Fig. 10. In these cases, n_H^T data exhibit a plateau that indicates the presence of a degenerate layer, in the 30–40 K and 20–40 K range, respectively. To eliminate this contribution by using Eqs. (A1)–(A3), it has been assumed that the residual conductivity of the highly degenerate surface layer fully accounts for the measured Hall mobility, μ_{exp} , and Hall carrier sheet concentration, $n_{exp, sheet}$, at 30 K and 20 K for samples C and C', respectively. If that is the case, neither the measured mobility nor the measured carrier concentration has to be corrected for r_H in the temperature range mentioned above.³⁹ Secondly, both μ_{exp} and $n_{exp, sheet}$ have been considered constant all over the temperature range scanned during the measurements, as theoretically expected.³⁹ It is worth noting that an exact estimate of the degenerate surface layer extension, d_{deg} , is not crucial for determining the implanted layer electrical characteristics since the actual key quantities in Eqs. (A1) and (A2) are the sheet carrier concentrations and mobilities. However, to compare the present approximation with the results reported in the literature, an upper bound for d_{deg} has also been calculated by considering as uniform the carrier concentration, $n_{deg}(T)$, in the degenerate layer. Then, since the Fermi level, E_F , is expected to be pinned at or above E_C , an upper bound for d_{deg} can be calculated as

$$d_{deg} \leq \frac{n_{exp, sheet}}{n_{deg}(T)|_{E_F=E_C}}, \quad (\text{A4})$$

where $n_{deg}(T)$ is evaluated according to

$$n_{deg}(T) = \int_{E_C}^{+\infty} \frac{(m^*)^{3/2}}{\pi^2 \hbar^3} \sqrt{2(E - E_C)} \frac{1}{e^{(E - E_C)/k_B T} + 1} dE, \quad (\text{A5})$$

with \hbar being the reduced Planck constant, while T is set equal to 30 K and 20 K for C and C', respectively.

The percentage correction to the Hall measurements due to the presence of the degenerate layer obtained by using the values listed in Table VI for μ_{exp} , $n_{exp, sheet}$, and d_{deg} are shown in Fig. 11. It can be seen that the surface conduction is dominating at temperature below ~ 50 K, as expected. On the contrary, at higher temperatures, the degenerate layer contribution to the overall measurements is progressively reducing since the Hall carrier concentration and

TABLE VI. The mobility μ_{exp} , sheet carrier concentration, $n_{exp,sheet}$, extension of the degenerate layer, d_{deg} , and extension of the H or ^2H implanted layer, d_{impl} , used to perform the multilayer analysis.

| Sample | μ_{exp} ($\text{cm}^2 \text{V}^{-1} \text{s}^{-1}$) | $n_{exp,sheet}$ (cm^{-2}) | d_{deg} (nm) | d_{impl} (μm) |
|--------|--|---|-------------------|---------------------------------|
| B | | | | 2.9 ± 0.3 |
| C | 47 ± 4 | $(2.1 \pm 0.1) \times 10^{11}$ | 23 ± 2 | 3.6 ± 0.4 |
| B' | | | | 4.3 ± 0.4 |
| C' | 27 ± 4 | $(2.2 \pm 0.3) \times 10^{11}$ | 40 ± 10 | 5.7 ± 0.6 |

Hall mobility of the underlying layers are significantly increasing and it is $\lesssim 2\%$ at RT, in agreement with previous studies.^{71,82}

The values reported in the literature for the surface layer mobility in HT-ZnO at low temperature vary in the

$\sim 7\text{--}16 \text{ cm}^2 \text{V}^{-1} \text{s}^{-1}$ range.⁸¹ More recently, an upper room temperature limit of $\approx 30 \text{ cm}^2 \text{V}^{-1} \text{s}^{-1}$ has been determined by quantitative mobility spectrum analysis using magnetic fields up to 35 T by Allen *et al.*⁸² These findings are in excellent agreement with the μ_{exp} values found here (see Table VI). The same holds for the estimates of $n_{exp,sheet}$, even though values ≈ 1 order of magnitude higher have been observed as well.⁸¹ On the contrary, the d_{deg} range is about ten times larger compared to previous report.^{81,82} This suggests that E_F might be considerably above E_C in our case. However, it is important to underline that experimental evidence of the presence of such a layer has been found only in C and C', i.e., the samples with the highest implanted [H] and [^2H]. Furthermore, this also indicates that introduction of the additional annealing for 30 min in air at 200 °C does not affect its presence. Hence, the present results are suggesting that residual implantation damage and/or H itself might play a relevant role in the formation of a degenerate layer as it was also concluded after forming gas annealing.⁸⁷ Therefore, the agreement found with previous published results, where the degenerate surface layer presence has been attributed to accumulation of extrinsic donors near the surface,⁸⁴ residual surface adsorbed species,⁸⁸ or intrinsic defects,⁸⁹ might be purely accidental and a more detailed investigation is required.

2. Substrate contribution

The H and ^2H chemical profiles in samples B, C, and B', C' are shown in Figs. 1(a) and 1(b), respectively. As mentioned in Subsection III B, the depth interval, where the conditions $[\text{H}] > [\text{Li}]$ and $[\text{H}] > [\text{Li}]$ hold, have been assumed as estimates for d_{impl} in samples B-C and B'-C', respectively. Then, these values, also reported in Table VI, have been used to extract the Hall mobility and the Hall carrier concentration of the H and ^2H implanted layers through Eq. (A1)–(A3), while assuming the remaining part of the samples electrically equal to the corresponding reference A or A'. The percentage of the substrate contributions to the overall Hall measurements is shown in Fig. 11. The largest correction on the low temperature side (150 K) is occurring to sample B and it accounts for $\sim 0.01\%$ and $\sim 0.005\%$ of the overall Hall carrier concentration and Hall mobility, respectively. This justifies the assumption of neglecting, in the implanted samples, any substrate influence to the Hall measurements performed at lower temperatures than the ones achievable in the case of A and A'. On the other hand, as the temperature raises, the substrate contribution is progressively increasing with a strong dependence on the implanted layer vs substrate relative electrical characteristics. Since $[\text{H}]$ is $\approx [\text{Li}]$ in sample B [see Fig. 1(a)], the carrier concentration normalized to the wafer thickness appears to be dominated by the substrate contribution for temperatures above ~ 270 K. That is, in this case at 330 K, the measured Hall carrier concentration is only $\sim 15\%$ larger than in A. Here, it is also worth mentioning that, for sample B at temperatures ≥ 290 K, the physical inequality $\mu_H^T n_H^T d_T > \mu_H^j n_H^j d_j$ necessary to obtain positive values for μ_H^i and n_H^i is not satisfied over the whole μ_H^T , n_H^T , μ_H^j , and n_H^j error ranges. Hence, the extraction of the H implanted layer electrical properties has been performed under the assumption of a minimum substrate contribution, that is, in this case the minimum Hall mobility and Hall carrier concentration of sample A within the error range have been used as values for μ_H^i and n_H^i , respectively.

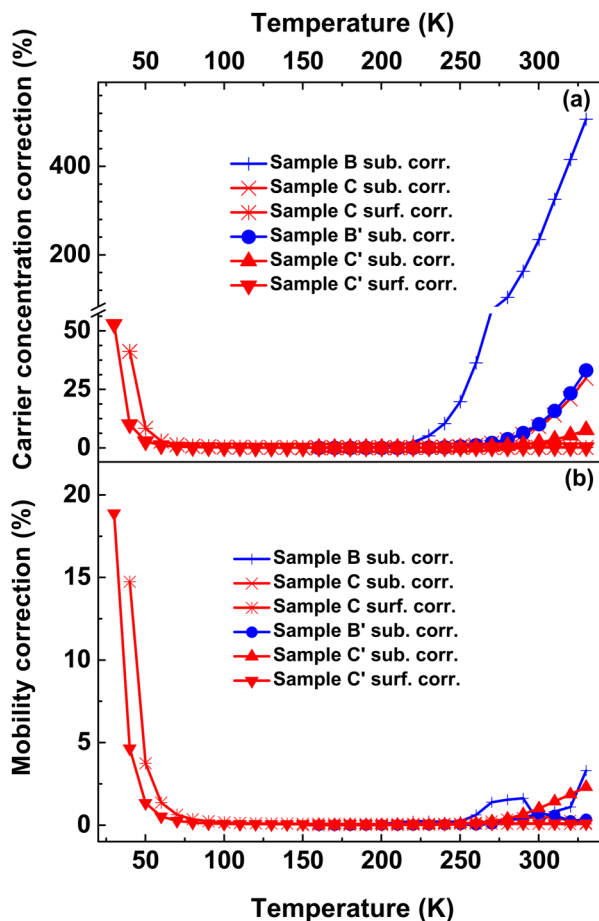


FIG. 11. Percentage surface layer and substrate contribution to the overall (a) Hall carrier concentration and (b) Hall mobility measurements. As discussed in the text, the surface layer correction has been performed only for samples C and C', since, only in this case, the experimental evidence for the presence of residual surface conduction has been found.

REFERENCES

- ¹C. V. de Walle, *Phys. Rev. Lett.* **85**, 1012 (2000).
- ²E. Mollwo, *Z. Phys.* **138**, 478 (1954).
- ³A. R. Hutson, *Phys. Rev.* **108**, 222 (1957).
- ⁴D. G. Thomas and J. J. Lander, *J. Chem. Phys.* **25**, 1136 (1956).
- ⁵A. Janotti and C. G. V. de Walle, *Nature Mater.* **6**, 44 (2007).
- ⁶E. V. Lavrov, F. Herklotz, and J. Weber, *Phys. Rev. B* **79**, 165210 (2009).
- ⁷D. M. Hofmann, A. Hofstaetter, F. Leiter, H. Zhou, F. Henecker, B. K. Meyer, S. B. Orlinskii, J. Schmidt, and P. G. Baranov, *Phys. Rev. Lett.* **88**, 045504 (2002).
- ⁸D. C. Look, G. C. Farlow, P. Reunchan, S. Limpijumnong, S. B. Zhang, and K. Nordlund, *Phys. Rev. Lett.* **95**, 225502 (2005).
- ⁹G. H. Kassier, M. Hayes, F. D. Auret, M. Diale, and B. G. Svensson, *Phys. Status Solidi (c)* **5**, 569 (2008).
- ¹⁰C. H. Seager and S. M. Myers, *J. Appl. Phys.* **94**, 2888 (2003).
- ¹¹Z. Zhang, D. C. Look, R. Schifano, K. M. Johansen, B. G. Svensson, and L. J. Brillson, *J. Phys. D Appl. Phys.* **46**, 055107 (2013).
- ¹²B. K. Meyer, H. Alves, D. M. Hofmann, W. Kriegseis, D. Forster, F. Bertram, J. Christen, A. Hoffmann, M. Straßburg, M. Dworzak, U. Habocek, and A. V. Rodina, *Phys. Status Solidi (b)* **241**, 231 (2004).
- ¹³G. A. Shi, M. Stavola, S. J. Pearton, M. Thieme, E. V. Lavrov, and J. Weber, *Phys. Rev. B* **72**, 195211 (2005).
- ¹⁴P. T. Neuvonen, L. Vines, B. G. Svensson, and A. Y. Kuznetsov, *Phys. Rev. Lett.* **110**, 015501 (2013).
- ¹⁵M. G. Wardle, J. P. Goss, and P. R. Briddon, *Phys. Rev. B* **72**, 155108 (2005).
- ¹⁶Y. K. Frodason, K. M. Johansen, T. S. Bjørheim, B. G. Svensson, and A. Alkauskas, *Phys. Rev. B* **97**, 104109 (2018).
- ¹⁷J. L. Lyons, J. B. Varley, D. Steiauf, A. Janotti, and C. G. V. de Walle, *J. Appl. Phys.* **122**, 035704 (2017).
- ¹⁸E. V. Lavrov, J. Weber, F. Börrnert, C. G. V. de Walle, and R. Helbig, *Phys. Rev. B* **66**, 165205 (2002).
- ¹⁹F. Herklotz, E. V. Lavrov, V. Kolkovskiy, J. Weber, and M. Stavola, *Phys. Rev. B* **82**, 115206 (2010).
- ²⁰F. Herklotz, A. Hupfer, K. M. Johansen, B. G. Svensson, S. G. Koch, and E. V. Lavrov, *Phys. Rev. B* **92**, 155203 (2015).
- ²¹J. Bang, Y.-S. Kim, C. H. Park, F. Gao, and S. B. Zhang, *Appl. Phys. Lett.* **104**, 252101 (2014).
- ²²Z. Q. Chen, A. Kawasuso, Y. Xu, N. Naramoto, X. L. Yuan, T. Sekiguchi, R. Suzuki, and T. Ohdaira, *Phys. Rev. B* **71**, 115213 (2005).
- ²³A threshold displacement energy of 57 eV for both Zn and O sublattices was used for the TRIM simulations.
- ²⁴See <http://www.srim.org/> for more information about TRIM.
- ²⁵J. M. Meese and D. R. Locker, *Solid State Commun.* **11**, 1547 (1972).
- ²⁶D. C. Look, J. W. Hemsky, and J. R. Sizelove, *Phys. Rev. Lett.* **82**, 2552 (1999).
- ²⁷R. Schifano, E. V. Monakhov, J. S. Christensen, A. Y. Kuznetsov, and B. G. Svensson, *Phys. Status Solidi (a)* **205**, 1998 (2008).
- ²⁸O. Schmidt, A. Geis, P. Kiesel, C. G. V. de Walle, N. M. Johnson, A. Bakin, A. Waag, and G. H. Döhler, *Superlattice Microstruct.* **39**, 8 (2006).
- ²⁹J. F. Muth, R. M. Kolbas, A. K. Sharma, S. Oktyabryskiy, and J. Narayan, *J. Appl. Phys.* **85**, 7884 (1999).
- ³⁰R. Schifano, E. V. Monakhov, L. Vines, B. G. Svensson, W. Mtangi, and F. D. Auret, *J. Appl. Phys.* **106**, 043706 (2009).
- ³¹T. R. Waite, *Phys. Rev.* **107**, 463 (1957).
- ³²T. R. Waite, *J. Chem. Phys.* **28**, 103 (1958).
- ³³M. S. Janson, A. Hallén, M. K. Linnarson, and B. G. Svensson, *Phys. Rev. B* **64**, 195202 (2001).
- ³⁴L. Vines, E. V. Monakhov, R. Schifano, W. Mtangi, F. D. Auret, and B. G. Svensson, *J. Appl. Phys.* **107**, 103707 (2010).
- ³⁵R. Schifano, E. V. Monakhov, B. G. Svensson, W. Mtangi, P. J. J. van Rensburg, and F. D. Auret, *Physica B* **404**, 4344 (2009).
- ³⁶K. M. Johansen, L. Vines, T. S. Bjørheim, R. Schifano, and B. G. Svensson, *Phys. Rev. Appl.* **3**, 024003 (2015).
- ³⁷J. E. Stehr, K. M. Johansen, T. S. Bjørheim, L. Vines, B. G. Svensson, W. M. Chen, and I. A. Buyanova, *Phys. Rev. Appl.* **2**, 021001 (2014).
- ³⁸J.-Y. Noh, H. Kim, Y.-S. Kim, and C. H. Park, *J. Appl. Phys.* **113**, 153703 (2013).
- ³⁹H. Morkoç, *Handbook of Nitride Semiconductors and Devices* (Wiley-VCH, Weinheim, 2008).
- ⁴⁰W. Shan, W. Walukiewicz, J. W. Ager, K. M. Yu, Y. Zhang, S. S. Mao, R. Kling, C. Kirchner, and A. Waag, *Appl. Phys. Lett.* **86**, 153117 (2005).
- ⁴¹F. Bertazzi, E. Bellotti, E. Furno, and M. Goano, *J. Electron. Mater.* **38**, 1677 (2009).
- ⁴²L. M. Falicov and M. Cuevas, *Phys. Rev.* **164**, 1025 (1967).
- ⁴³K. Seeger, *Semiconductor Physics*, Springer Series in Solid State Sciences Vol. 40 (Springer, Berlin, Heidelberg, 1997).
- ⁴⁴C. F. Klingshirn, B. K. Meyer, A. Waag, A. Hoffmann, and J. Geurts, *Zinc Oxide, From Fundamental Properties Towards Novel Applications* (Springer-Verlag, Berlin, 2010), Chap. 7.
- ⁴⁵J. R. Haynes, *Phys. Rev. Lett.* **4**, 361 (1960).
- ⁴⁶B. Svensson, T. M. Børseth, K. M. Johansen, T. Maqsood, R. Schifano, U. Grossner, J. S. Christensen, L. Vines, P. Klason, Q. X. Zhao, M. Willander, F. Tuomisto, W. Skorupa, E. V. Monakhov, and A. Kuznetsov, *Mater. Res. Soc. Symp. Proc.* **1035**, L04-01 (2008).
- ⁴⁷K. M. Johansen, H. Haug, Ø. Prytz, P. T. Neuvonen, K. E. Knutsen, L. Vines, E. V. Monakhov, A. Y. Kuznetsov, and B. G. Svensson, *J. Electron. Mater.* **40**, 429 (2011).
- ⁴⁸K. M. Johansen, A. Zubiaga, I. Makkonen, F. Tuomisto, P. T. Neuvonen, K. E. Knutsen, E. V. Monakhov, A. Y. Kuznetsov, and B. G. Svensson, *Phys. Rev. B* **83**, 245208 (2011).
- ⁴⁹D. G. Thomas, *J. Phys. Chem. Solids* **3**, 229 (1957).
- ⁵⁰A. Janotti and C. G. V. de Walle, *Phys. Rev. B* **76**, 165202 (2007).
- ⁵¹A. Carvalho, A. Alkauskas, A. Pasquarello, A. K. Tagantsev, and N. Setter, *Phys. Rev. B* **80**, 195205 (2009).
- ⁵²G. Y. Huang, C. Y. Wang, and J. T. Wang, *J. Phys. Condens. Matter* **21**, 345802 (2009).
- ⁵³Both O and Zn face have been checked in the case of sample A, while charging effects prevent to perform accurate SIMS measurements in the case of sample A'.
- ⁵⁴M. G. Wardle, J. P. Goss, and P. R. Briddon, *Phys. Rev. B* **71**, 155205 (2005).
- ⁵⁵K. M. Johansen, J. S. Christensen, E. V. Monakhov, A. Y. Kuznetsov, and B. G. Svensson, *Appl. Phys. Lett.* **93**, 152109 (2008).
- ⁵⁶In similar samples, a V_{Zn} concentration of $\sim 2 \times 10^{15} \text{ cm}^{-3}$ has been measured by positron annihilation spectroscopy. Considering that V_{Zn} presents the lowest formation energy in the *n*-type ZnO, the equilibrium concentrations of the intrinsic point defect are considered negligible.
- ⁵⁷N. H. Nickel, *Phys. Rev. B* **73**, 195204 (2006).
- ⁵⁸K. E. Knutsen, K. M. Johansen, P. T. Neuvonen, B. G. Svensson, and A. Y. Kuznetsov, *J. Appl. Phys.* **113**, 023702 (2013).
- ⁵⁹J. J. Lander, *J. Phys. Chem. Solids* **15**, 324 (1960).
- ⁶⁰A. Catellani and A. Calzolari, *Materials* **10**, 332 (2017).
- ⁶¹K. M. Johansen, H. Haug, E. Lund, E. V. Monakhov, and B. G. Svensson, *Appl. Phys. Lett.* **97**, 211907 (2010).
- ⁶²K. S. Chan, L. Vines, K. M. Johansen, E. V. Monakhov, J. D. Ye, P. Parkinson, C. Jagadish, B. G. Svensson, and J. Wong-Leung, *J. Appl. Phys.* **114**, 083111 (2013).
- ⁶³E. G. Seebauer and M. C. Kratzer, *Charged Semiconductor Defects* (Springer-Verlag, 2009).
- ⁶⁴R. Schifano, E. Monakhov, U. Grossner, and B. G. Svensson, *Appl. Phys. Lett.* **91**, 193507 (2007).
- ⁶⁵G. H. Kassier, M. Hayes, F. D. Auret, M. Mamor, and K. Bouziane, *J. Appl. Phys.* **102**, 014903 (2007).
- ⁶⁶F. D. Auret, S. A. Goodman, M. J. Legodi, W. E. Meyer, and D. C. Look, *Appl. Phys. Lett.* **80**, 1340 (2002).
- ⁶⁷J. Monecke, W. Siegel, E. Ziegler, and G. Kühnel, *Phys. Status Solidi (b)* **103**, 269 (1981).
- ⁶⁸B. Pódör, *Semicond. Sci. Technol.* **2**, 177 (1987).

- ⁶⁹In sample C', since N_{D1} is ~ 2 orders of magnitude larger than N_{D2} , $n_{imp}(T)$ is dominated by D_1 , thus preventing to extract E_{D2} in this case.
- ⁷⁰A. Hupfer, C. Bhoodoo, L. Vines, and B. G. Svensson, *Mater. Sci. Semicond. Process.* **69**, 13 (2017).
- ⁷¹D. C. Look, *J. Appl. Phys.* **104**, 063718 (2008).
- ⁷²M. Schumm, "ZnO-based semiconductors studied by Raman spectroscopy: Semimagnetic alloying, doping, and nanostructures," Ph.D. thesis (der Julius Maximilians Universität Würzburg, 2009).
- ⁷³E. V. Kortunova, N. G. Nikolaeva, P. P. Chvanski, V. V. Maltsev, E. A. Volkova, E. V. Koporulina, N. I. Leonyuk, and T. F. Kuech, *J. Mater. Sci.* **43**, 2336 (2008).
- ⁷⁴F. Tuomisto, K. Saarinen, D. C. Look, and G. C. Farlow, *Phys. Rev. B* **72**, 085206 (2005).
- ⁷⁵M. Schilling, R. Helbig, and G. Pensl, *J. Lumin.* **33**, 201 (1985).
- ⁷⁶J. K. Dangbégnon, K. Talla, and J. R. Botha, *Opt. Mater.* **34**, 920 (2009).
- ⁷⁷J.-K. Lee, M. Nastasi, D. W. Hamby, and D. A. Lucca, *Appl. Phys. Lett.* **86**, 171102 (2005).
- ⁷⁸B. K. Meyer, J. Sann, and A. Zeuner, *Superlattice Microstruct.* **38**, 344 (2005).
- ⁷⁹R. Chwang, B. J. Smith, and C. R. Crowell, *Solid-State Electron.* **17**, 1217 (1974).
- ⁸⁰B. Arnaudov, T. Paskova, S. Evtimova, E. Valcheva, M. Heuken, and B. Monemar, *Phys. Rev. B* **67**, 045314 (2003).
- ⁸¹D. C. Look, *Surf. Sci.* **601**, 5315 (2007).
- ⁸²M. W. Allen, C. H. Swartz, T. H. Myers, T. D. Veal, C. F. McConville, and S. M. Durbin, *Phys. Rev. B* **81**, 075211 (2010).
- ⁸³R. Schifano, E. V. Monakhov, B. G. Svensson, and S. Diplas, *Appl. Phys. Lett.* **94**, 132101 (2009).
- ⁸⁴D. C. Look, B. Clafin, and H. E. Smith, *Appl. Phys. Lett.* **92**, 122108 (2008).
- ⁸⁵S. Brochen, C. Granier, G. Feuillet, and J. Pernot, *Appl. Phys. Lett.* **100**, 052115 (2012).
- ⁸⁶G. H. Kassier, "The characterization of bulk as-grown and annealed ZnO by the Hall effect," Master thesis (University of Pretoria, 2007).
- ⁸⁷D. C. Look, *Superlattice Microstruct.* **42**, 284 (2007).
- ⁸⁸B. J. Coppa, R. F. Davis, and R. J. Nemanich, *Appl. Phys. Lett.* **82**, 400 (2003).
- ⁸⁹L. J. Brillson, Y. Dong, D. Doust, D. C. Look, and Z.-Q. Fang, *Physica B* **404**, 4768 (2009).